

# POLITECNICO DI TORINO

Master's Degree in Electronic Micro and Nanosystem



Master's Degree Thesis

## "Design and Control of a Miniature Indoor Blimp: A Safer, Quieter, and Resilient Alternative for Indoor Exploration and Surveillance"

Supervisors

Prof. Carla Fabiana CHIASSERINI

Candidate

Marco PELLEGRINO

07 2023





# Table of Contents

<b>List of Figures</b>	v
<b>1 Background and Research Objectives</b>	4
1.1 Background . . . . .	4
1.2 State of the art . . . . .	5
<b>2 Modelling of the Dynamic</b>	9
2.1 Introduction . . . . .	9
2.2 Assumptions . . . . .	9
2.3 Kinematic and Dynamic modelling . . . . .	10
2.3.1 Choise of Inertial and Body Frames . . . . .	10
2.3.2 Rotational Matrix and convention . . . . .	11
2.3.3 Kinematic model . . . . .	12
2.3.4 Dynamic Model . . . . .	14
2.4 Simplified Model . . . . .	22
2.4.1 Schematic structure of the blimp understudy . . . . .	23
2.4.2 Assumptions for simplified model . . . . .	25
2.4.3 Simplified altitude movement model . . . . .	26
2.4.4 Simplified planar movement model . . . . .	27
2.4.5 Conclusion . . . . .	30
<b>3 Design and Implementation</b>	32
3.1 Sensors . . . . .	33
3.1.1 Crazyflie Bolt . . . . .	34
3.1.2 Motion Capture System . . . . .	36

3.2	State Estimation with Kalman Filter . . . . .	37
3.2.1	Prediction Step . . . . .	38
3.2.2	Update Step . . . . .	38
3.2.3	Final Process . . . . .	39
3.2.4	Work Done . . . . .	40
3.3	PID Controller . . . . .	40
3.3.1	Controller Design Considerations . . . . .	41
3.4	Power Distribution . . . . .	43
3.4.1	Output of the Controller and scaling . . . . .	44
3.5	Propeller Analysis, Linearization, and Battery Compensation . . . . .	46
3.5.1	Propeller Analysis . . . . .	47
3.5.2	Battery Compensation and Linearization . . . . .	52
3.6	Chapter Summary and Conclusion . . . . .	59
<b>4</b>	<b>Design Processes, Result and Performance Evaluation</b>	<b>63</b>
4.1	Design and Prototyping . . . . .	64
4.1.1	Initial Design and Prototyping . . . . .	64
4.1.2	Iterative Design changes . . . . .	66
4.2	Tuning Process . . . . .	71
4.2.1	Development of the Python Script . . . . .	71
4.2.2	Theoretical Basis for Tuning . . . . .	71
4.3	Detailed Examination of Autonomous Flight Outcomes . . . . .	72
4.3.1	Trajectory Analysis . . . . .	72
4.3.2	Altitude Maintenance . . . . .	74
4.3.3	Flight Duration . . . . .	75
4.3.4	Robustness and Scalability . . . . .	75
4.3.5	Real-world Applicability . . . . .	75
4.3.6	Limitations . . . . .	76
4.3.7	Future Work . . . . .	77
	<b>Bibliography</b>	<b>82</b>

# List of Figures

1.1	General classification for aircraft . . . . .	6
2.1	Reference frame for indoor blimp robots. . . . .	10
2.2	Motor configuration for the blimp . . . . .	24
3.1	Description of the motion capture system Qualisys . . . . .	37
3.2	Cascaded PID Controller schematization in the crazyflie firmware [Source: <a href="https://www.bitcraze.io/documentation/repository/crazyflie-firmware/master/functional-areas/sensor-to-control/controllers/cascaded-pid-controller">https://www.bitcraze.io/documentation/repository/crazyflie-firmware/master/functional-areas/sensor-to-control/controllers/cascaded-pid-controller</a> ] . . . . .	42
3.3	Schematization of the PID Controlled used for the blimp . . . . .	43
3.4	Studied propellers (from left to right): 2-Blade 40mm, Smooth 4-Blade 40mm, Rigid 4-Blade 40mm, 3-Blade 31mm. . . . .	49
3.5	Measurement setup: A precision scale is positioned beneath a structure to which the propeller-attached motor is mounted. The generated thrust is inferred from the change in recorded weight. . . . .	50
3.6	Thrust generated by different propellers as a function of applied command. On the Y-axis there is the Thrust[g], on the X-axis there is the Command . . . . .	51
3.7	Current draw by different propellers as a function of generated thrust. On the Y-axis, there is the current draw [A]; on the X-axis, there is the generated thrust [g]. . . . .	51
3.8	A 3D scatter plot depicting the system's behaviour as a function of the command and voltage. This plot offers an overall view demonstrating the interaction between variables. . . . .	53

3.9	An alternate view of the 3D scatter plot, focusing on the Command-Thrust plane, which validates our previous propeller analysis measurements. . . . .	54
3.10	The 3D scatter plot of the back spinning direction, with a surface plot of the regression result superimposed. . . . .	55
3.11	The 3D scatter plot of the forward spinning direction, with a surface plot of the regression result superimposed. . . . .	56
3.12	Thrust output as a function of battery voltage for a fixed command without compensation. The thrust significantly drops as the battery discharges. . . . .	58
3.13	Thrust output as a function of battery voltage for a fixed command with battery compensation. Despite the battery discharging, the thrust remains nearly constant. . . . .	59
3.14	Changes in command values as a function of battery voltage to maintain near-constant thrust. The compensation algorithm adjusts the command values dynamically to ensure consistent performance. . . . .	60
3.15	Post-compensation thrust as a function of command and battery voltage, showing a linear behaviour. The superimposed 1-degree plane surface serves to underscore the linearization achieved. . . . .	61
4.1	This first prototype has been made by a rearranging of the motor of a Crazyflie . . . . .	65
4.2	This prototype has the first one made with a crazyflie Bolt . . . . .	67
4.3	This image represent the trajectory made by a blimp and a nano quadcopter without involving the use of the Qualisys system. . . . .	68
4.4	3D model of the lower motor support. The design allows for flexibility to conform to the shape of the hull and minimize oscillations during motor operation. . . . .	69
4.5	3D model of the lateral motor support. . . . .	69
4.6	Final prototype of the blimp understudy. . . . .	70
4.7	Squared Trajectory of the Blimp . . . . .	73
4.8	Altitude Variation over Time . . . . .	74



# Introduction

Unmanned aerial vehicles (UAVs), particularly quadcopters, have emerged as key players in diverse fields such as surveillance, logistics, and environmental research. Their versatility and agility notwithstanding, quadcopters present a multitude of challenges. In indoor environments, these challenges become especially pronounced due to safety risks associated with fast-spinning rotors, inability to recover from collisions, and a considerable amount of noise generated. This thesis introduces an innovative unmanned aerial platform—the miniature indoor blimp—carefully designed to navigate these challenges while preserving high performance levels.

A blimp, also known as an airship, is a type of lighter-than-air craft that navigates through the air under its own power. Blimps, unlike balloons, maintain their shape even when the internal pressure is reduced. Their envelopes are filled with a gas lighter than air, typically helium, which provides the necessary lift for the craft to float and manoeuvre with minimal energy. The miniature indoor blimp discussed in this thesis is designed to be small and lightweight, making it suitable for indoor navigation.

Among the many advantages the indoor blimp holds over traditional quadcopters, the ability to remain airborne for extended periods is particularly striking. This endurance is primarily enabled by the lift provided by helium. Helium, being lighter than air, ensures the blimp can float, thereby requiring minimal energy expenditure. It also enhances the blimp’s resilience to minor impacts. The extended flight time afforded by the blimp introduces new possibilities for executing long-duration tasks, which are typically challenging for other UAVs due to their energy constraints.

Moreover, when it comes to safety, the blimp significantly outperforms traditional UAVs. Its inherent ability to tolerate collisions and the quieter operational noise level make it an especially appealing option for indoor navigation. These features

considerably enhance the safety aspect of indoor aerial navigation, a domain where quadcopters often fall short.

Beyond these compelling advantages, this thesis delves deeper into two crucial technical enhancements that contribute to the indoor blimp's superior performance—position control and trajectory following. These features, inherent in quadcopters, are not only preserved in the design of the blimp but have been adapted and optimised to complement its unique attributes.

The blimp's position control system is one such adaptation. Developed based on the principles of control theory and studying the state-of-the-art, this system endows the blimp with the ability to move and hover with impressive accuracy. This accurate control and stability make it an excellent candidate for tasks requiring precision and steadiness.

Similarly, the blimp's capability to follow a specific trajectory is another function that has been finessed in our design. This critical function, integral to its autonomous navigation system, enables the blimp to follow a path accurately. It is an invaluable feature for tasks such as indoor surveillance, where the same path needs to be followed repeatedly, or exploration tasks where the blimp must navigate through unknown environments.

In addition to these features, our blimp design incorporates a machine learning-based obstacle avoidance system. This system enables the blimp to 'learn' and adapt to its environment over time, thereby improving its efficacy in indoor navigation tasks. It significantly reduces the risk of collisions and enhances both the safety and reliability of the blimp, broadening its scope of application.

While a comparative study with quadcopters forms an integral part of this thesis, the main focus is the design intricacies and control capabilities of the indoor blimp. The thesis chronicles the journey from the blimp's conceptualisation to its final implementation, capturing the technicalities, challenges, and triumphs encountered along the way.

In conclusion, this thesis offers a comprehensive exploration of the potential of miniature blimps as indoor exploration vehicles. It delves deep into their advantages over traditional quadcopters, focusing on superior spatial control, trajectory-following capabilities, extended flight times, and increased safety features. The ultimate aim is to contribute to the broader discourse on UAVs and to inspire

further research and innovation in the field of safer, quieter, and more resilient indoor aerial vehicles.

# Chapter 1

## Background and Research Objectives

This chapter delves into the background of blimps, highlighting their historical significance and exploring the motivation behind the research conducted in this study. It provides an overview of the current state of the art in blimp technology. Additionally, the chapter examines the dynamics of blimps and emphasizes the crucial role of design in ensuring the optimal functionality of the device under investigation.

### 1.1 Background

Blimps, also known as airships or dirigibles, have a rich history and have fascinated humans for over a century. Unlike aeroplanes or helicopters that rely on aerodynamic lift, these lighter-than-air vehicles use the principle of buoyancy to fly.

The first models of airships have been made back in the 19th century with a rigid and semi-rigid structure and laid the foundation for subsequent development in the field.

Throughout the 20th century, blimps had crucial roles in various fields: they were used for military purposes, as platforms for surveillance or as an offensive weapon during World War I and World War II, but also as luxurious transportation vehicles.

Blimp also has historical significance in terms of its use in scientific exploration and research. From the first missions to explore Earth's atmosphere to more recent weather and climate research, blimps have enabled scientists to gather valuable data and expand our understanding of the world.

Furthermore, blimps have found applications in advertising, with their large surface area offering a unique opportunity for companies to display their brands and messages in the sky. These aerial billboards have become a familiar sight at major events and in city skylines.

However, despite their historical significance and diverse applications, traditional blimps have faced challenges when it comes to precise positional control, especially in three-dimensional space. This limitation has motivated the need for smaller blimps that can navigate and maintain position in indoor environments, opening up new possibilities for exploration, monitoring, and manoeuvrability.

## **1.2 State of the art**

Generally, the control of mobile robots involves several different aspects, from the perception of environmental information to the localization on the map, then according to the mission, a path is planned for the robot to follow by applying motion control.

Flying machines are always been very interesting for humans, and researchers in these years started to study them with much more interest UAVs. Unmanned aerial vehicles (UAVs) are aircraft that operate without a pilot onboard, controlled either manually via remote control or autonomously through computer systems. UAVs find applications across various fields, including military operations, cargo transportation, and surveillance [1]. They come in different design configurations tailored for specific use cases. Two commonly encountered designs are the quadcopter and aeroplane configurations.

In general, aerial vehicles can be classified into Heavier-Than-Air(HTA) and Lighter-Than-Air(LTA) categories. Starting from this, many sub-categories can be defined depending on the flying principle and the propulsion mode. as shown in fig. 1.1.

In this work, we try to give a non-exhaustive comparison of the different flying

principles between the most common types of aircraft by explaining briefly the motivation of our choice.

The quadcopter configuration features a compact body propelled by four independent propellers. This design allows for quick manoeuvrability and the ability to move in any direction. However, the constant spinning of the propellers for flight consumes a significant amount of energy, making it less energy-efficient.

On the other hand, the aeroplane configuration consists of a fuselage equipped with wings. This design allows for higher speeds and longer-distance travel due to its method of generating lift. However, changing direction with an aeroplane requires forward movement coupled with rolling or pitching motions, which reduces its overall agility. Moreover is not able at all to achieve indoor exploration and cannot perform vertical take-off and landing (VTOL).

In summary, UAVs offer versatile capabilities, with the quadcopter design excelling in agility but at the cost of energy consumption, while the aeroplane design offers speed and efficiency over longer distances but sacrifices some manoeuvrability.

To address the issue of high energy consumption in the quadcopter configuration, a potential solution is to incorporate characteristics of a buoyant blimp into its

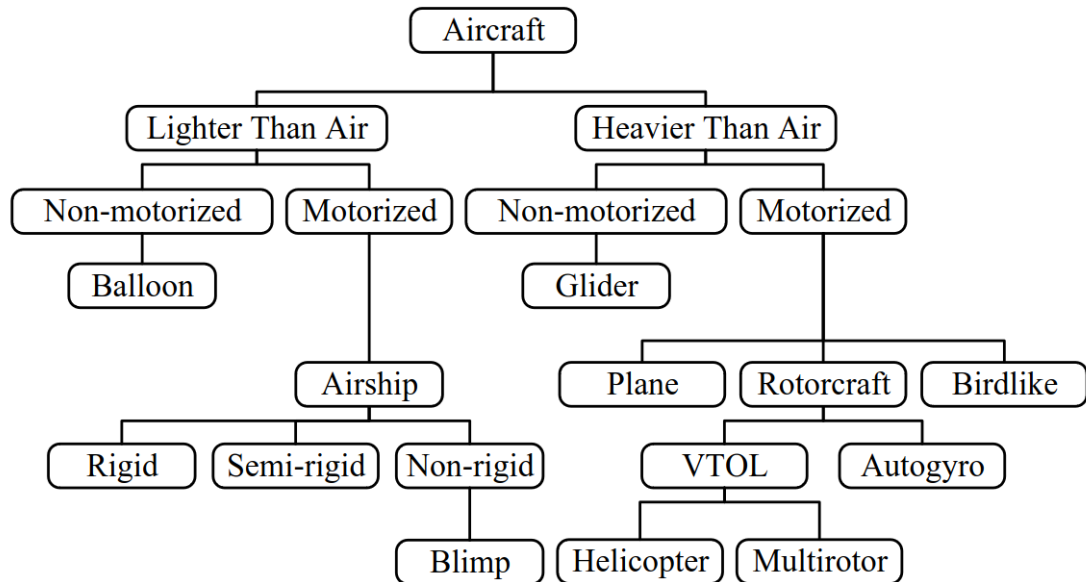


**Figure 1.1:** General classification for aircraft

design.

In this work, we focus on the blimp, which is a non-rigid airship, different from semi-rigid and rigid (one of the most common models of the rigid airship was the Zeppelin) because it maintains the shape by the pressure of the lifting gas inside.

So far, there have been limited research endeavours dedicated to the design of airships. However, several relevant papers addressing the subject matter of this study will be discussed in the following.

A blimp or airship is an aircraft that utilizes lighter-than-air gases confined within its body to generate buoyancy [2]. By combining the quadcopter with a blimp-like structure, a UAV can harness buoyancy to maintain flight with minimal energy input while retaining the capability to manoeuvre in all directions. This hybrid design offers the advantage of energy-efficient flight and omnidirectional movement at the expense of an increase in dimensions.

Most blimps designed for UAV applications follow the classic airship structure, featuring an oval shape, actuated by thrusters which are mounted on a gondola, and limited movement capabilities primarily focused on forward motion and movement along an arc of circumference. While this design approach offers advantages in terms of reduced hardware complexity and weight, it is important to note that these blimps typically lack precise position control systems.

The simplified design of these blimps, optimized for low-resolution point-to-point navigation rather than trajectory following, allows for a considerable reduction in hardware components. By minimizing the number of components, such as control surfaces and additional propellers, the weight and overall size of the blimp can be significantly reduced. This reduction in size can be advantageous in scenarios where compactness and ease of deployment are critical factors.

However, due to the absence of dedicated position control systems, such blimps are generally unable to maintain precise positions in three-dimensional space or follow specific trajectories. Their movement is primarily governed by factors such as wind currents and natural buoyancy adjustments. Consequently, their operational capabilities are more suited for applications where reaching a specific point in space without strict trajectory requirements is sufficient.

While these classic airship-based blimps may lack advanced position control, they can still find utility in certain scenarios. For instance, they can serve as aerial

platforms for basic surveillance, aerial photography, or environmental monitoring where approximate location information is sufficient.

It is important to recognize that the trade-off for reduced hardware complexity and size in these blimps comes at the expense of precise position control and trajectory-following capabilities. Therefore, for applications requiring more accurate positioning or trajectory tracking, alternative designs or additional control systems may need to be considered.

In the existing literature, there is a noticeable scarcity of attempts to develop devices that fulfill the specific requirements mentioned earlier. While there have been advancements in the field of aerial robotics and unmanned systems, few studies have specifically focused on achieving these particular specifications in the context of a compact blimp. One notable paper in this domain is the work by Murri et al. [3], which introduces the concept of an "Omnidirectional Blimp" capable of flight with six degrees of freedom. However, the dimensions of this spherical blimp, measuring 2.7 meters in diameter, are considerably larger compared to the compact design of the device under consideration in this study. This highlights the unique nature and novelty of the present research, as it aims to develop a smaller blimp that meets the requirements of precise position control and trajectory following. By addressing this research gap, the outcomes of this study, building upon previous work and considering the specific constraints of a smaller form factor, can contribute valuable insights and advancements to the field of aerial robotics, expanding the possibilities for indoor exploration and maneuverability while ensuring safety and control.

# Chapter 2

## Modelling of the Dynamic

### 2.1 Introduction

The motion of a blimp, as every UAVs, can be described by its dynamic model. Starting from the airship nonlinear model [4], a simplified form can be derived. Due to the complexity of the airship dynamic, which could require lots of experiments to identify all the parameters, we can stay under certain assumptions and the complex model can be decoupled into independent parts, allowing to ease the design of the motion controller and estimators. This chapter starts with the modelling of the blimp in the next two sections and goes into the simplification of this model in the following ones.

### 2.2 Assumptions

The model described in this chapter is based on certain assumptions due to the fact that we are working on an indoor platform that behaves differently from an eventual outdoor one.

- The density of the blimps is approximately or slightly more than air allowing the blimp to stay in the air without (or with little) actuator actions.
- Even if we considered a non-rigid airship we neglect the aeroelastic behaviour of the hull, so we consider the device as a rigid airship.

- The blimp moves at low speed.
- The internal movement of the added fluid due to the motion is neglected.
- The indoor blimp does not have any kind of ballonnet to adjust the inner pressure and buoyancy, so the mass and the volume are considered to be constant.
- The air viscosity is constant.
- The hull is considered as an ellipsoid.

## 2.3 Kinematic and Dynamic modelling

In this section, we are going to describe accurately a simplified dynamic model of the airship based on the work on Gomes [5].

### 2.3.1 Choise of Inertial and Body Frames

The reference frame for describing the blimp model is in fig.2.1.

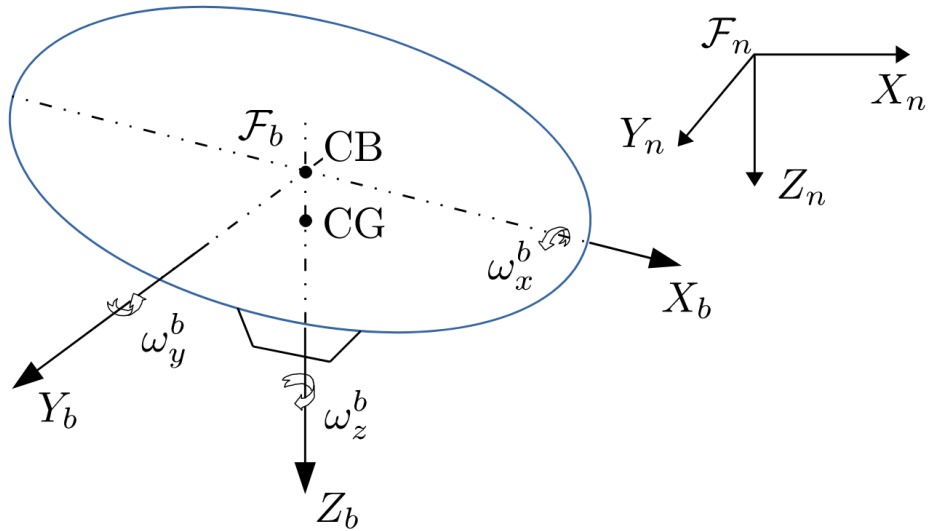


**Figure 2.1:** Reference frame for indoor blimp robots.

The frame  $\mathcal{F}_n$  is tangent with the earth, we suppose that, due to the nature of the indoor application, the movement of the Earth is ignored so  $\mathcal{F}_n$  is considered as an inertial frame. The frame  $\mathcal{F}_b$  is located in the centre volume (CV) of the hull. In this model, we are considering the gondola and all the component that regards the controlling part are in the bottom part of the blimp, so we can consider that the centre of gravity (CG) is located on the  $\mathbf{Z}_b$  axis, therefore in  $\mathcal{F}_b$  the coordinate of the CG is  $r_G^b = [0 \ 0 \ z_G]^T$ .

In  $\mathcal{F}_b$  the instantaneous linear and angular velocities are described as:

$$\xi^b = [(v^b)^T \ (\omega^b)^T]^T = [v_x^b \ v_y^b \ v_z^b \ \omega_x^b \ \omega_y^b \ \omega_z^b]^T$$

whereas the position and the orientation expressed with the respect of  $\mathcal{F}_n$  are expressed as

$$\eta^n = [(\eta_1^n)^T \ (\eta_2^n)^T]^T = [x^n \ y^n \ z^n \ \phi \ \theta \ \psi]^T$$

### 2.3.2 Rotational Matrix and convention

Define  $\mathbf{R}_{\mathcal{F}}^{\mathcal{F}'}$  as the rotation matrix from fram  $\mathcal{F}$  to  $\mathcal{F}'$ . We chose the  $z - y' - x''$  angle convention to transform from the inertial frame  $\mathcal{F}_n$  to the body-fixed frame  $\mathcal{F}_b$ , that means that  $\mathcal{F}_n$  is rotated firstly by an angle  $\psi$  (yaw) around  $\mathbf{Z}_n$ -axis to an intermediate frame  $\mathcal{F}_1$ , the rotation matrix from  $\mathcal{F}_n$  to  $\mathcal{F}_1$  is

$$\mathbf{R}_n^1 = \begin{bmatrix} \cos \psi & -\sin \psi & 0 \\ \sin \psi & \cos \psi & 0 \\ 0 & 0 & 1 \end{bmatrix}$$

then this frame is rotated around the  $\mathbf{Y}'$ -axis by an angle  $\theta$ (pitch) to obtain the frame  $\mathcal{F}_2$ , the rotation matrix from  $\mathcal{F}_1$  to  $\mathcal{F}_2$  is

$$\mathbf{R}_1^2 = \begin{bmatrix} \cos \theta & 0 & \sin \theta \\ 0 & 1 & 0 \\ -\sin \theta & 0 & \cos \theta \end{bmatrix}$$

finally the frame is rotated around the  $\mathbf{X}''$ -axis by an angle  $\theta$ (pitch) to obtain the frame  $\mathcal{F}_b$ , the rotation matrix from  $\mathcal{F}_2$  to  $\mathcal{F}_3$  is

$$\mathbf{R}_2^b = \begin{bmatrix} 1 & 0 & 0 \\ 0 & \cos \phi & -\sin \phi \\ 0 & \sin \phi & \cos \phi \end{bmatrix}$$

So the final rotation matrix from  $\mathcal{F}_n$  to  $\mathcal{F}_b$  is

$$\mathbf{R}_n^b = \mathbf{R}_n^1 \mathbf{R}_1^2 \mathbf{R}_2^b \quad (2.1)$$

and any vector  $\mathbf{u}$  can be defined in the inertial frame as

$$\mathbf{u}^n = \mathbf{R}_n^b \mathbf{u}^b \quad (2.2)$$

### 2.3.3 Kinematic model

As described in the 2.3.1 the change of reference system equation for the instantaneous linear velocity is

$$\mathbf{v}^n = \dot{\eta}_1^n = \begin{bmatrix} \dot{x}^n & \dot{y}^n & \dot{z}^n \end{bmatrix}^T = \mathbf{R}_n^b \mathbf{v}^b = \mathbf{R}_n^b \begin{bmatrix} v_x^b & v_y^b & v_z^b \end{bmatrix}^T \quad (2.3)$$

that could be written as

$$\dot{\eta}_1^n = \mathbf{R}_n^b(\eta_1^n) \mathbf{v}^b \quad (2.4)$$

where

$$\mathbf{R}_n^b(\eta_2^n) = \begin{bmatrix} \cos \psi \cos \theta & \cos \psi \sin \phi \sin \theta - \cos \phi \sin \psi & \sin \phi \sin \psi + \cos \phi \cos \psi \sin \theta \\ \cos \theta \sin \psi & \cos \phi \cos \psi + \sin \phi \sin \psi \sin \theta & \cos \phi \sin \psi \sin \theta - \cos \psi \sin \phi \\ -\sin \theta & \cos \theta \sin \phi & \cos \phi \cos \theta \end{bmatrix} \quad (2.5)$$

For the rotational kinematic equation  $\omega$  the rotation matrix is

$$\dot{\mathbf{R}}_n^b = \mathbf{R}_n^b S(\omega^b) \quad (2.6)$$

where the operator  $S(\cdot)$  is defined as follows:

The exterior product of two vectors  $x = \begin{bmatrix} x_1 & x_2 & x_3 \end{bmatrix}^T$ ,  $y = \begin{bmatrix} y_1 & y_2 & y_3 \end{bmatrix}^T$  denoted by  $x \wedge y$  is defined by:

$$\begin{aligned}
 x \wedge y &= \begin{bmatrix} x_1 \\ x_2 \\ x_3 \end{bmatrix} \wedge \begin{bmatrix} y_1 \\ y_2 \\ y_3 \end{bmatrix} = \begin{bmatrix} x_2 y_3 - x_3 y_2 \\ x_3 y_1 - x_1 y_3 \\ x_1 y_2 - x_2 y_1 \end{bmatrix} \\
 &= -y \wedge x \\
 &= S(x)y
 \end{aligned}$$

where the skew-symmetric (i.e.  $S = -S^T$ ) matrix  $S$  is defined by

$$S(x) = \begin{bmatrix} 0 & -x_3 & x_2 \\ x_3 & 0 & -x_1 \\ -x_2 & x_1 & 0 \end{bmatrix}$$

So the angular velocity of frame  $\mathcal{F}_b$  with respect to  $\mathcal{F}_n$  and expressed in body-fixed frame is

$$S(\omega^b) = (\mathbf{R}_n^b)^T \dot{\mathbf{R}}_n^b \quad (2.7)$$

knowing that the rotational matrix is such that  $(\mathbf{R}_n^b)^T = (\mathbf{R}_n^b)^{-1}$ .

Using the eq.2.5 to solve the eq.2.6 and then combining the coefficient with respect to  $\dot{\phi}$ ,  $\dot{\theta}$  and  $\dot{\psi}$ , we obtain:

$$\begin{bmatrix} \omega_x^b \\ \omega_y^b \\ \omega_z^b \end{bmatrix} = \begin{bmatrix} 1 & 0 & -\sin \theta \\ 0 & \cos \phi & \cos \theta \sin \phi \\ 0 & -\sin \phi & \cos \theta \cos \phi \end{bmatrix} \begin{bmatrix} \dot{\phi} \\ \dot{\theta} \\ \dot{\psi} \end{bmatrix} \quad (2.8)$$

and from the inversion of this equation we can obtain the vector related to the angular speed referred to the inertial frame:

$$\dot{\eta}_2^n = T_n^b(\eta_2^n) \omega^b = \begin{bmatrix} 1 & \sin \phi \tan \theta & \cos \phi \tan \theta \\ 0 & \cos \phi & -\sin \phi \\ 0 & \sin \phi / \cos \theta & \cos \phi / \cos \theta \end{bmatrix} \omega^b \quad (2.9)$$

The matrix  $T_n^b(\eta_2^n)$  has singularities at  $\theta = (2k+1)\frac{\pi}{2}$  due to the the limit of euler angles. This problem could be solved by using quaternions which is a description of the orientation that uses 4 parameters. But in our case, the blimp motion is such that the pitch angle will not reach the singularity condition.

Summarising:

$$\begin{bmatrix} \dot{\eta}_1^n \\ \dot{\eta}_2^n \end{bmatrix} = \begin{bmatrix} \mathbf{R}_n^b(\eta_2^n) & \mathbf{0}_{3 \times 3} \\ \mathbf{0}_{3 \times 3} & \mathbf{T}_n^b(\eta_2^n) \end{bmatrix} \begin{bmatrix} \mathbf{v}^b \\ \boldsymbol{\omega}^b \end{bmatrix} \quad (2.10)$$

or

$$\dot{\eta}^n = J(\eta^n) \xi^b \quad (2.11)$$

### 2.3.4 Dynamic Model

In this section the commonly used dynamic model designed for indoor blimp robot is presented. The blimp is depicted in fig.2.1. To establish the relation between the blimp's accelerations and the forces and moments acting on it, the Newton-Euler equation of motion is used [Fossen, 1994; Gomes, 1990; Zufferey et al., 2006]. Moreover due to the fact that the dynamics of the blimp is similar to the dynamics of underwater vehicles [Fossen, 1994; Gomes, 1999], the added-inertia effects are taken into account, and it is shown that the 6-DOF nonlinear dynamic equations of the blimp motion can be expressed as

$$\mathbf{M} \dot{\xi}^b + \mathbf{C}(\xi^b) \xi^b + \mathbf{D}(\xi^b) \xi^b + \mathbf{g}(\eta^n) = \boldsymbol{\tau}^b \quad (2.12)$$

where the terms are:

- $\mathbf{M}$  : the inertia matrix, containing the blimp inertia, and added-inertia terms;
- $\mathbf{C}(\xi^b)$  : the matrix of the Coriolis and centripetal terms, which are fictitious forces due to the description of the blimp motion in non-inertial frame  $\mathcal{F}_b$ ;
- $\mathbf{g}(\eta^n)$  : the vector of restoring forces and moments, including the gravity of the whole robot and the buoyancy generated by helium gas in the balloon, they are responsible for keeping the blimp upright;
- $\boldsymbol{\tau}^b$  : the vector of control inputs, which is used to describe the propulsion forces and moments generated by actuators acting on the blimp in the body-fixed frame.

These terms are presented below.

### Restoring Forces and moments

The blimp's lifting force is achieved through aerostatic means, indicating that it remains unaffected by the speed of its flight, thanks to the presence of helium gas within the balloon. According to Archimedes' principle, the buoyancy force of the blimp is equivalent to the weight of the air displaced by the balloon. Figure 2.1 illustrates that, due to the installation of the gondola beneath the balloon, the center of gravity (CG) is positioned below the center of buoyancy (CB). In practical terms, the combined forces of buoyancy  $f_B$  and gravity  $f_G$  work together to maintain the airship in an upright position, hence referred to as the restoring force.

In addition the gravitational force  $f_G$  acts on the  $CG$  which is at

$$\mathbf{r}_G^b = \begin{bmatrix} 0 & 0 & z_G \end{bmatrix}^T$$

of the blimp, and the buoyancy force  $f_B$  acts at the CB, which is the origin of  $\mathcal{F}_b$ , i.e.  $\mathbf{r}_B^b = \mathbf{0}_{3 \times 1}$ . By using the change of basis equation, in the body fixed frame there is:

$$\mathbf{f}_G^b = \mathbf{R}_b^n \mathbf{f}_G^n = (\mathbf{R}_n^b)^T \mathbf{f}_G^n = (\mathbf{R}_n^b)^T \begin{bmatrix} 0 \\ 0 \\ f_G \end{bmatrix}$$

Similarly

$$\mathbf{f}_B^b = (\mathbf{R}_n^b)^T \mathbf{f}_B^n = (\mathbf{R}_n^b)^T \begin{bmatrix} 0 \\ 0 \\ -f_B \end{bmatrix}$$

with

$$\begin{aligned} f_G &= mg, \\ f_B &= \rho_{\text{air}} V g, \\ V &= \frac{4}{3} \pi a b^2 \end{aligned}$$

where  $m$  is the mass of the blimp,  $g$  is the Earth gravitational acceleration,  $\rho_{\text{air}}$

is the air density, and  $V$  is the volume of ellipsoid shape balloon with semi-axes  $a$  and  $b$ . Consequently, the restoring forces and moment vector in  $\mathcal{F}_b$  is

$$\mathbf{g}(\eta^n) = - \begin{bmatrix} f_G^b + f_B^b \\ r_G^b \wedge f_G^b + r_B^b \wedge f_B^b \end{bmatrix} \quad (2.13)$$

Notice that the sign of  $\mathbf{g}(\eta)$  must be changed since it appears on the left-hand side of the Newton's Second Law, see (2.10). Explicitly

$$\mathbf{g}(\eta^n) = - \begin{bmatrix} -(f_G - f_B) \sin \theta \\ (f_G - f_B) \cos \theta \sin \phi \\ (f_G - f_B) \cos \theta \cos \phi \\ -z_G f_G \cos \theta \sin \phi \\ -z_G f_G \sin \theta \\ 0 \end{bmatrix} \quad (2.14)$$

### Propulsion forces and moments

As previously discussed, small indoor blimps typically rely on motor-propeller combinations to generate propulsive forces. This is due to the inefficiency of control surfaces such as the rudder and elevator at low flight speeds. However, the specific configuration of thrusters, including their number, mounting positions, and orientations, can vary depending on the application. Consequently, the propulsion forces and moments vector  $\tau^b$  differ among different types of blimp robots.

In most studies concerning indoor blimp robots, the motors are assumed to be ideal, meaning their effects are directly proportional to the commands they receive. Additionally, for the sake of simplicity in modelling, the propeller fluxes and motor torques are often disregarded. As a result, the propulsion forces  $\tau^b$  are dependent solely on the motor commands and the motor installation. For the purpose of clarity, we will use the following notation to represent the term  $\tau^b$ .

$$\tau^b = \begin{bmatrix} f_{px} & f_{py} & f_{pz} & \tau_{px} & \tau_{py} & \tau_{pz} \end{bmatrix}^T \quad (2.15)$$

## Damping forces and moments

The aerodynamic damping of a blimp is influenced by the air friction it encounters. Generally, air friction can be categorized into two types: laminar flow, where the drag force is directly proportional to the velocity, and turbulent flow, where the drag force is proportional to the squared velocity. In the study conducted by [Fossen, 1994], the researchers examined the damping forces and moments experienced by a slowly moving underwater vehicle. They simplified the model by disregarding terms beyond the second order and proposed a diagonal structure for the variable  $D(\xi^b)$ .

$$D(\xi^b) = -\text{diag} \begin{bmatrix} D_{v_x} + D_{v_x^2} \left| v_x^b \right| \\ D_{v_y} + D_{v_y^2} \left| v_y^b \right| \\ D_{v_z} + D_{v_z^2} \left| v_z^b \right| \\ D_{\omega_x} + D_{\omega_x^2} \left| \omega_x^b \right| \\ D_{\omega_y} + D_{\omega_y^2} \left| \omega_y^b \right| \\ D_{\omega_z} + D_{\omega_z^2} \left| \omega_z^b \right| \end{bmatrix} \quad (2.16)$$

Where  $D_{v_x}, D_{v_y}, D_{v_z}, D_{\omega_x}, D_{\omega_y}, D_{\omega_z}$  are the linear damping coefficients, and  $D_{v_x^2}, D_{v_y^2}, D_{v_z^2}, D_{\omega_x^2}, D_{\omega_y^2}, D_{\omega_z^2}$  are the quadratic damping coefficients. According to the authors, the uncoupled damping model 2.16 works well in case of low speed and highly symmetrical ellipsoid hull [Fossen, 1994].

## Inertia Matrix

The inertia matrix  $\mathbf{M}$  contains both the rigid body (RB) inertia  $\mathbf{M}_{\text{RB}}$  and the added inertia  $\mathbf{M}_{\text{Added}}$ . The rigid body inertia matrix can be written as [Fossen, 1994]

$$\mathbf{M}_{\text{RB}} = \begin{bmatrix} m\mathbf{I}_{3 \times 3} & -mS(\mathbf{r}_G^b) \\ mS(\mathbf{r}_G^b) & \mathbf{I}_{\text{RB}} \end{bmatrix}. \quad (2.17)$$

Additionally, we have the moment of inertia matrix, denoted as  $\mathbf{I}_{\text{RB}}$ , which pertains to the rotational motion around the center of mass, specifically with respect to point  $CB$ . It is essential to remember that  $r_G^b$  signifies the coordinate of the center of gravity in the reference frame  $\mathcal{F}_b$ , while  $S(\cdot)$  represents the operator

for generating a skew-symmetric matrix. Notably, the robot exhibits symmetry in two planes, namely the  $xz$ -plane and the  $yz$ -plane. As a result, we can simplify the rigid body inertia matrix as described in the work by Fossen [1994] as

$$\mathbf{M}_{\text{RB}} = \begin{bmatrix} m & 0 & 0 & 0 & mz_G & 0 \\ 0 & m & 0 & -mz_G & 0 & 0 \\ 0 & 0 & m & 0 & 0 & 0 \\ 0 & -mz_G & 0 & I_x & 0 & 0 \\ mz_G & 0 & 0 & 0 & I_y & 0 \\ 0 & 0 & 0 & 0 & 0 & I_z \end{bmatrix} \quad (2.18)$$

Now, let's direct our attention towards the increased inertia of the blimp. To enable the blimp's movement through the air, the robot must displace certain amounts of the surrounding fluid. This occurrence significantly affects the blimp, as it is a buoyant vehicle with a density comparable to that of the air. Consequently, this phenomenon creates an illusion of greater inertia for the blimp compared to its measured value, which is not considered in the conventional rigid body inertia matrix (2.18).

The additional effect is modelled as added-inertia, including added-mass and added moment of inertia. Under the assumption that the indoor blimp robot moves slowly and it has three planes of symmetry for the ellipsoid shape hull, the added-inertia can be expressed as

$$\mathbf{M}_{\text{Added}} = \text{diag} \begin{bmatrix} m_{A_x} \\ m_{A_y} \\ m_{A_z} \\ I_{A_x} \\ I_{A_y} \\ I_{A_z} \end{bmatrix} \quad (2.19)$$

Then the global inertia matrix  $\mathbf{M}$  is derived as the sum of  $\mathbf{M}_{\text{RB}}$  and added-inertia matrix  $\mathbf{M}_{\text{Added}}$

$$\mathbf{M} = \mathbf{M}_{\text{RB}} + \mathbf{M}_{\text{Added}} = \begin{bmatrix} m'_x & 0 & 0 & 0 & mz_G & 0 \\ 0 & m'_y & 0 & -mz_G & 0 & 0 \\ 0 & 0 & m'_z & 0 & 0 & 0 \\ 0 & -mz_G & 0 & I'_x & 0 & 0 \\ mz_G & 0 & 0 & 0 & I'_y & 0 \\ 0 & 0 & 0 & 0 & 0 & I'_z \end{bmatrix} \quad (2.20)$$

where

$$\begin{cases} m'_x = m + m_{A_x} \\ m'_y = m + m_{A_y} \\ m'_z = m + m_{A_z} \\ I'_x = I_x + I_{A_x} \\ I'_y = I_y + I_{A_y} \\ I'_z = I_z + I_{A_z} \end{cases} \quad (2.21)$$

The identification of  $M$  primarily focuses on the diagonal elements, while the components of  $\mathbf{MRB}$  can be easily determined through experiments. The remaining portion corresponds to added inertia. According to the research conducted by [Munk, 1934], the added mass is the product of fluid density and a specific volume. The volume solely relies on the geometric characteristics of the blimp. This leads to the derivation of Lamb's  $k$ -factors, denoted as  $k_1$  and  $k_2$ , which represent the inertia coefficients of the portion of mass displaced by the hull. Additionally,  $k'$  denotes the ratio between the added moment of inertia and the moment of inertia of the air displaced by the hull, denoted as  $I_{z_h}$  [Lamb, 1932]. When considering an ellipsoidal hull with semi-axes  $a$  and  $b$  (where  $a \geq b$ ), the value of  $I_{z_h}$  can be determined using [Fossen, 1994].

$$I_{z_h} = \frac{4}{15} \pi \rho a b^2 (a^2 + b^2)$$

Then the added-inertia can be calculated by using the Lamb's  $k$ -factors

$$\begin{cases} m_{A_x} = k_1 m \\ m_{A_y} = m_{A_z} = k_2 m \\ I_{A_x} = 0 \\ I_{A_y} = I_{A_z} = k' I_{z_h} \end{cases}$$

where the Lamb's  $k$ -factors are defined by

$$\begin{cases} k_1 = \frac{\alpha_0}{2-\alpha_0} \\ k_2 = \frac{\beta_0}{2-\beta_0} \\ k' = \frac{e^4(\beta_0-\alpha_0)}{(2-e^2)[2e^2-(2-e^2)(\beta_0-\alpha_0)]} \\ \alpha_0 = \frac{2(1-e^2)}{e^3} \left( \frac{1}{2} \ln \frac{1+e}{1-e} - e \right) \\ \beta_0 = \frac{1}{e^2} - \frac{(1-e^2)}{2e^3} \ln \frac{1+e}{1-e} \end{cases}$$

where  $e$  denotes the ellipsoid eccentricity

$$e = \sqrt{1 - \left(\frac{b}{a}\right)^2}$$

Note that a spherical hull has 50% added-mass in all the directions and no added moment of inertia (when  $a/b = 1$ ,  $k_1 = k_2 = 0.5$ , and  $k' = 0$ ), and as the shape tends to be elongated, the longitudinal added-mass ( $k_1$ ) decreases, the lateral added-mass and added moment of inertia ( $k_2$  and  $k'$ ) increase.

### Coriolis and centripetal forces and moments

The Coriolis and centripetal forces are considered as fictional forces because they arise from the description of the blimp's movement in a non-inertial reference frame as  $\mathcal{F}b$ . The Coriolis force is directly proportional to both the angular velocity and the linear velocity. It acts in a direction perpendicular to both the rotation axis and the blimp's velocity vector. On the other hand, the centripetal force is proportional to the square of the angular velocity and the distance between the blimp's center of gravity (CG) and the axis of rotation in the frame  $\mathcal{F}b$ .

Both of these forces can be represented in the body-fixed frame as the term  $C(\xi^b)\xi^b$ , where  $C(\xi^b)$  is referred to as the Coriolis matrix. According to the findings of Sagatun and Fossen in 1991, the Coriolis matrix can be directly derived

from the inertia matrix.

$$C(\xi^b) = \begin{bmatrix} \mathbf{0}_{3 \times 3} & -S(\mathbf{M}_{11}\mathbf{v}^b + \mathbf{M}_{12}\omega^b) \\ -S(\mathbf{M}_{11}\mathbf{v}^b + \mathbf{M}_{12}\omega^b) & -S(\mathbf{M}_{21}\mathbf{v}^b + \mathbf{M}_{22}\omega^b) \end{bmatrix} \quad (2.22)$$

where  $\mathbf{M}_{ij}(i, j = 1, 2)$  are the four  $3 \times 3$  sub-matrices of the global inertia matrix  $\mathbf{M}$ . The explicit form of  $C(\xi^b)$  is

$$C(\xi^b) = - \begin{bmatrix} 0 & 0 & 0 & 0 & -m'_z v_z & m'_y v_y - m z_G \omega_x \\ 0 & 0 & 0 & m'_z v_z & 0 & -m'_x v_x - m z_G \omega_y \\ 0 & 0 & 0 & -m'_y v_y + m z_G \omega_x & m'_x v_x + m z_G \omega_y & 0 \\ 0 & -m'_z v_z & m'_y v_y - m z_G \omega_x & 0 & -I'_z \omega_z & m z_G v_x + I'_y \omega_y \\ m'_z v_z & 0 & -m'_x v_x - m z_G \omega_y & I'_z \omega_z & 0 & m z_G v_y - I'_x \omega_x \\ -m'_y v_y + m z_G \omega_x & m'_x v_x + m z_G \omega_y & 0 & -m z_G v_x - I'_y \omega_y & -m z_G v_y + I'_x \omega_x & 0 \end{bmatrix} \quad (2.23)$$

According to a study conducted by Zufferey et al. in 2006, the inherent instability of a hull-shaped blimp's axial motion can be attributed to the Coriolis and centripetal forces. The discrepancy between  $m'_x$  and  $m'_y$  leads to a yaw moment induced by the vector  $C(\xi^b)\xi^b$  formed by the Coriolis and centripetal forces. Even a slight angle between the  $X_b$ -axis (which represents the blimp's forward direction) and the direction of motion tends to amplify this instability, as noted by Munk in 1936.

This instability is directly proportional to the difference between the lateral and longitudinal Lamb's  $k$ -factors ( $k_2 - k_1$ ).

To summarize, the added-inertia phenomenon accounts for the observed discrepancy between the blimp's apparent inertia, which is higher than the measured inertia  $\mathbf{M}_{RB}$ . This phenomenon also explains undesired effects such as yawing moments that occur when the blimp moves forward, as discussed by Zufferey et al. in 2006.

Thus far, we have presented the dynamic model of the indoor blimp robot, along with its constituent elements, including the restoring forces, propulsion forces, damping matrix, inertia matrix, and Coriolis and centripetal matrix.

To summarize, the 6-DOF dynamic model of the blimp is written as

$$\begin{aligned}
 m'_x \dot{v}_x^b + m \dot{\omega}_y^b z_G - \omega_z^b (m'_y v_y^b - m \omega_x^b z_G) + m'_z \omega_y^b v_z^b - v_x^b (D_{v_x} + D_{v_z^2} |v_x^b|) + (f_G - f_B) \sin \theta &= f_{px} \\
 m'_y \dot{v}_y^b - m \dot{\omega}_x^b z_G + \omega_z^b (m'_x v_x^b + m \omega_y^b z_G) - m'_z \omega_x^b v_z^b - v_y^b (D_{v_y} + D_{v_z^2} |v_y^b|) - (f_G - f_B) \cos \theta \sin \phi &= f_{py} \\
 m'_z \dot{v}_z^b + \omega_x^b (m'_y v_y^b - m \omega_x^b z_G) - \omega_y^b (m'_x v_x^b + m \omega_y^b z_G) - v_z^b (D_{v_z} + D_{v_z^2} |v_z^b|) - (f_G - f_B) \cos \theta \cos \phi &= f_{pz} \\
 I'_x \dot{\omega}_x^b - m \dot{v}_y^b z_G + I'_z \omega_y^b \omega_z^b - v_z^b (m'_y v_y^b - m \omega_x^b z_G) - \omega_z^b (I'_y \omega_y^b + m v_x^b z_G) + m'_z v_y^b v_z^b - \omega_x^b (D_{\omega_x} + D_{\omega_x^2} |\omega_x^b|) + z_G f_G \cos \theta \sin \phi &= \tau_{px} \\
 I'_y \dot{\omega}_y^b + m \dot{v}_x^b z_G - I'_z \omega_x^b \omega_z^b + v_z^b (m'_x v_x^b + m \omega_y^b z_G) + \omega_z^b (I'_x \omega_x^b - m v_y^b z_G) - m'_z v_x^b v_z^b - \omega_y^b (D_{\omega_y} + D_{\omega_y^2} |\omega_y^b|) + z_G f_G \sin \theta &= \tau_{py} \\
 I'_z \dot{\omega}_z^b + v_x^b (m'_y v_y^b - m \omega_x^b z_G) - v_y^b (m'_x v_x^b + m \omega_y^b z_G) + \omega_x^b (I'_y \omega_y^b + m v_x^b z_G) - \omega_y^b (I'_x \omega_x^b - m v_y^b z_G) - \omega_z^b (D_{\omega_z} + D_{\omega_z^2} |\omega_z^b|) &= \tau_{pz}
 \end{aligned} \tag{2.24}$$

## 2.4 Simplified Model

The commonly utilized indoor blimp dynamic model exhibits a complex structure (2.24). Researchers strive to develop a model that closely emulates real-world scenarios. However, this endeavour necessitates a substantial amount of precise experimental data to accurately determine the parameters. Nevertheless, certain terms cannot be precisely modelled. Let us now explore some of these challenges.

One notable issue pertains to the inaccurate assumption of the blimp hull's ellipsoid shape. Consequently, Lamb's  $k$ -factors for calculating added inertia must be ascertained based on the specific hull shape. This task can prove even more intricate and may require costly equipment such as a wind tunnel to conduct real-world tests and obtain reliable data. Another assumption made during dynamic modelling is the disregard for the airflow generated by the motor propellers. However, in our case, this approximation fails to capture the true nature of the situation. The motors used to propel a blimp also produce airflow that passes near the hull, significantly impacting aerodynamic effects such as the drag forces depicted in the complex model.

Furthermore, the model assumes constant values for air properties, including temperature, pressure, and density. Nonetheless, in indoor environments, these air properties are observed to vary easily, exerting a significant influence on the buoyancy force, hull internal pressure, and other characteristics of the blimp robot. For example, if the testing room is exposed to sunlight, the temperature will rise (akin to a greenhouse effect), causing a decrease in air density and subsequently reducing the blimp's buoyancy force.

Moreover, given the focus on an indoor blimp robot in this study, it becomes

imperative for the robot to be sufficiently compact and have limited carrying capacity. Consequently, this imposes restrictions on the number of sensors that can be mounted on the robot as well as the computational complexity of the control and estimation algorithms.

Hence, it becomes evident that the prevailing approach aims to construct an extremely precise dynamic model for the blimp, resulting in a complex structure that necessitates extensive experimentation and data collection to accurately identify its parameters. However, certain terms and disturbances remain unaccounted for in this approach. In contrast, our objective is to strike a balance between model complexity and accuracy by devising a modeling method that primarily addresses the motion control problem of the robot, while also ensuring robustness against disturbances. Additionally, due to resource constraints, we lack access to costly experimental equipment required for precise parameter identification.

To achieve this goal, we simplify the model further to establish a nominal model specifically for blimp motion control. This nominal model should be easily identifiable and capable of representing motion with an acceptable level of accuracy. Subsequently, we incorporate a disturbance term into the nominal model, which accounts for the disparity between the nominal model and the actual conditions. This term is estimated and compensated for in real-time by the controller. Consequently, we can ensure control accuracy while minimizing complexity.

### 2.4.1 Schematic structure of the blimp understudy

The structure of our blimp robot is present in fig.2.2. Two of the motors ( $\mathcal{M}_1$  and  $\mathcal{M}_4$ ) are mounted vertically in the plane  $\mathbf{O}_b\mathbf{Z}_b\mathbf{Y}_b$ , at symmetric position with respect to the  $X_b$ -axis, they are used as a first glance to adjust the altitude of the blimp. The other two motors ( $\mathcal{M}_2$  and  $\mathcal{M}_3$ ) are mounted horizontally in a plane parallel to  $\mathbf{O}_b\mathbf{X}_b\mathbf{Y}_b$ , and in the plane  $O_bY_bZ_b$ , at symmetric position with respect to the  $Z_b$ -axis.

In this work, the studied blimp robot has a balloon which has an ellipsoid like shape, with a length of 70 cm, a width of 80 cm, and the height is 80 cm, the balloon can carry a total weight of about 150 grams. The size of the blimp is miniature compared to other airships in the related works.

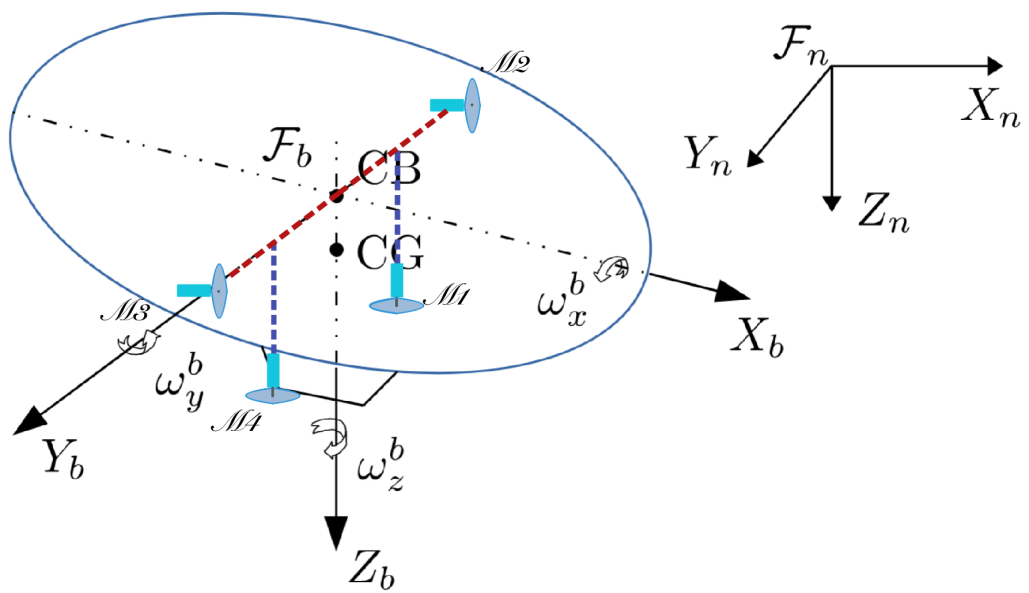


Figure 2.2: Motor configuration for the blimp

## 2.4.2 Assumptions for simplified model

Further assumptions are made in order to simplify the model of blimp for its motion control. The blimp is assumed to move at low speed, and it does not have high dynamic motion, therefore the following assumption is made: the blimp pitch  $\theta$  angle is fixed to zero during movement while the roll  $\phi$  angle is very small allowing to model the motion along the  $Y_b$ -axis as an effect of two counter forces applied on the CB.

Under these assumption, we have that  $\phi = \dot{\phi} = \theta = \dot{\theta} = 0$ . Substituting the terms into equation (2.8), there is

$$\begin{bmatrix} \omega_x^b \\ \omega_y^b \\ \omega_z^b \end{bmatrix} = \begin{bmatrix} 1 & 0 & 0 \\ 0 & 1 & 0 \\ 0 & 0 & 1 \end{bmatrix} \begin{bmatrix} \dot{\phi} \\ \dot{\theta} \\ \dot{\psi} \end{bmatrix}$$

Therefore it is clear that the angular velocities  $\omega_x^b = \omega_y^b = 0$ . Hence two DOF out of six are constrained, only the motions  $v_x^b, v_y^b, v_z^b$  and  $\omega_z^b$  are left to be studied.

From the 6DOF model, under those assumptions we can derive the simplified dynamic model:

$$\begin{aligned} m'_x \dot{v}_x^b - m'_y \omega_z^b v_y^b - v_x^b (D_{v_x} + D_{v_x^2} |v_x^b|) &= f_{px} \\ m'_y \dot{v}_y^b + m'_x \omega_z^b v_x^b - v_y^b (D_{v_y} + D_{v_y^2} |v_y^b|) &= f_{py} \\ m'_z \dot{v}_z^b - v_z^b (D_{v_z} + D_{v_z^2} |v_z^b|) + (f_B - f_G) &= f_{pz} \\ (m'_z - m'_y) v_y^b v_z^b - m z_G (\dot{v}_y^b + \omega_z^b v_x^b) &= \tau_{px} \\ (m'_x - m'_z) v_y^b v_z^b + m z_G (\dot{v}_x^b - \omega_z^b v_y^b) &= \tau_{py} \\ I'_z \dot{\omega}_z^b + (m'_y - m'_x) v_x^b v_y^b - \omega_z^b (D_{\omega_z} + D_{\omega_z^2} |\omega_z^b|) &= \tau_{pz} \end{aligned} \tag{2.25}$$

The fourth and fifth equations can be ignored since we are not interested in the pitch and roll motion of the blimp.

In addition, the blimp is assumed to move slowly, thus the damping coefficients are approximated by only the linear term, which leads to another assumption:

$$\mathbf{D}(\xi^b) = -\text{diag} \left( \begin{bmatrix} D_{v_x} & D_{v_y} & D_{v_z} & D_{\omega_x} & D_{\omega_y} & D_{\omega_z} \end{bmatrix}^T \right)$$

so the simplified model (2.25) can be further simplified to:

$$\begin{aligned}
 m'_x \dot{v}_x^b - m'_y \omega_z^b v_y^b - D_{v_x} v_x^b &= f_{px} \\
 m'_y \dot{v}_y^b + m'_x \omega_z^b v_x^b - D_{v_y} v_y^b &= f_{py} \\
 m'_z \dot{v}_z^b - D_{v_z} v_z^b + (f_B - f_G) &= f_{pz} \\
 I'_z \dot{\omega}_z^b + (m'_y - m'_x) v_x^b v_y^b - D_{\omega_z} \omega_z^b &= \tau_{pz}
 \end{aligned} \tag{2.26}$$

From the explicit representation of the simplified model (2.26), an observations can be made: the vertical movement (altitude) and the horizontal movement (in the plane) of the investigated blimp in this study can be decoupled, indicating their independence from each other and can be divided into two distinct sub-problems; these sub-problems can be individually analyzed, addressed, and combined to achieve comprehensive control over the blimp's motion.

### 2.4.3 Simplified altitude movement model

From the previous consideration it can be seen that the blimp movement in the vertical direction ( $Z_n$ ) can be considered independently, thus extracting from the equation (2.26), there is

$$m'_z \dot{v}_z^b - D_{v_z} v_z^b + (f_B - f_G) = f_{pz} \tag{2.27}$$

where  $m'_z$  is the apparent mass in the  $Z_n$  direction, it is not measured and the influence caused by the added-mass is considered in the parameter identification process.

In addition, from the kinematic model, the following relation is obtained

$$\dot{\eta}_1^n = \begin{bmatrix} \dot{x}^n \\ \dot{y}^n \\ \dot{z}^n \end{bmatrix} = \begin{bmatrix} \cos \psi & -\sin \psi & 0 \\ \sin \psi & \cos \psi & 0 \\ 0 & 0 & 1 \end{bmatrix} \begin{bmatrix} v_x^b \\ v_y^b \\ v_z^b \end{bmatrix} \tag{2.28}$$

thus there is  $\dot{z}^n = v_z^b$  and  $\ddot{z}^n = \dot{v}_z^b$ , recall that  $z^n$  is the altitude of the blimp

to the reference plane  $\mathbf{O}_n \mathbf{X}_n \mathbf{Y}_n$ , and the propulsive force  $f_{pz}$  is supposed to be proportional to square of motor rotation speed, which is modeled as the input. Then the equation can be transformed to get the simplified altitude movement dynamic model:

$$\ddot{z} = a_z \dot{z} + b_z u_z + c_z \quad (2.29)$$

In this context, the variable  $c_z$  represents the combined impact of buoyancy and gravity acting upon the blimp. On the other hand,  $a_z$  denotes the coefficient associated with air resistance, while  $b_z$  signifies the coefficient corresponding to the input  $u_z$ . For the sake of simplicity, we will omit the superscript  $(\cdot)^n$  when referring to the altitude  $z$  in this explanation. It is important to note that the command signal for the vertical motors,  $u_z$ , is a dimensionless quantity. Consequently, the parameter  $b_z$  shares the same unit as  $\ddot{z}$ .

#### 2.4.4 Simplified planar movement model

The blimp decoupled movement in the horizontal plane is modelled by the rest part of (2.26) :

$$\begin{aligned} m'_x \dot{v}_x^b - m'_y \omega_z^b v_y^b - D_{v_x} v_x^b &= f_{px} \\ m'_y \dot{v}_y^b + m'_x \omega_z^b v_x^b - D_{v_y} v_y^b &= f_{py} \\ I'_z \dot{\omega}_z^b + (m'_y - m'_x) v_x^b v_y^b - D_{\omega_z} \omega_z^b &= \tau_{pz} \end{aligned} \quad (2.30)$$

On the horizontal plane, the blimp has a configuration vector

$$\eta_{\text{Horiz}}^n = \begin{bmatrix} x^n & y^n & \psi \end{bmatrix}^T$$

and the instantaneous velocities vector

$$\xi_{\text{Horiz}}^b = \begin{bmatrix} v_x^b & v_y^b & \omega_z^b \end{bmatrix}^T$$

where  $v_x^b$  and  $v_y^b$  can also be called the lateral velocity and longitudinal velocity respectively.

Thus the kinematic equation of the blimp simplified horizontal movement is

$$\dot{\eta}_{\text{Horiz}}^n = J(\eta_{\text{Horiz}}^n) \xi_{\text{Horiz}}^b \quad (2.31)$$

where

$$J(\eta_{\text{Horiz}}^n) = \begin{bmatrix} \cos \psi & -\sin \psi & 0 \\ \sin \psi & \cos \psi & 0 \\ 0 & 0 & 1 \end{bmatrix}$$

Next, let us analyze the propulsion forces and moments  $f_{px}, f_{py}, \tau_{pz}$ , they are generated by the two motors  $\mathcal{M}_1$  and  $\mathcal{M}_3$  mounted horizontally as shown in Figure 2.3. Assume  $\mathcal{M}_1$  and  $\mathcal{M}_4$  generate propulsive forces  $f_{\text{rightxy}}$  and  $f_{\text{leftxy}}$  respectively.

$$\begin{cases} f_{px} = f_{\text{leftxy}} + f_{\text{rightxy}} \\ f_{py} = 0 \\ \tau_{pz} = (f_{\text{leftxy}} - f_{\text{rightxy}}) l \end{cases}$$

where  $l$  is the half distance between the two motors. As mentioned previously, we have assumed a roll angle of 0. However, we have the ability to manipulate the two motors, denoted as  $\mathcal{M}1$  and  $\mathcal{M}4$ , in order to generate a moment that facilitates motion along the ( $Y_b$ ) axis. To represent this movement, we can modify the system by introducing two hypothetical forces.

$$\begin{cases} f_{px} = f_{\text{leftxy}} + f_{\text{rightxy}} \\ f_{py} = f_{\text{leftyz}} - f_{\text{rightyz}} \\ \tau_{pz} = (f_{\text{leftxy}} - f_{\text{rightxy}}) l \end{cases}$$

Rearranging the blimp planar movement dynamic model (2.26) we get

$$\begin{cases} m'_x \dot{v}_x^b = m'_y v_y^b \omega_z^b + D_{v_x} v_x^b + f_{\text{leftxy}} + f_{\text{rightxy}} \\ m'_y \dot{v}_y^b = -m'_x v_x^b \omega_z^b + D_{v_y} v_y^b + f_{\text{leftyz}} - f_{\text{rightyz}} \\ I'_z \dot{\omega}_z^b = (m'_x - m'_y) v_x^b v_y^b + D_{\omega_z} \omega_z^b + (f_{\text{leftxy}} - f_{\text{rightxy}}) l \end{cases} \quad (2.32)$$

recall that  $m'_x, m'_y$  and  $I'_z$  are the apparent mass and moment with respect to different axis;  $D_{v_x}, D_{v_y}$  and  $D_{\omega_z}$  are the corresponding damping coefficients.

In the third equation, it can be seen that the difference between apparent mass in the lateral and longitudinal direction will cause an unstable yaw moment during

the moving forward motion. To simplify the dynamic model, recall that the blimp is supposed to move slowly, and the global mass terms  $m'_x$  and  $m'_y$  are assumed to be approximately equal, i.e.  $m'_x \approx m'_y = m_{\text{Horiz}}$ , thus this unstable yaw moment term disappears.

From equation (2.31) there is:

$$\begin{cases} \dot{x}^n = c_\psi v_x^b - s_\psi \dot{v}_y^b \\ \dot{y}^n = s_\psi v_x^b + c_\psi \dot{v}_y^b \end{cases}$$

where  $c_\psi = \cos \psi$ ,  $s_\psi = \sin \psi$  for simplicity of notation. Taking time-derivative on both sides:

$$\begin{cases} \ddot{x}^n = -s_\psi \dot{\psi} v_x^b + c_\psi \dot{v}_x^b - c_\psi \dot{\psi} v_y^b - s_\psi \dot{v}_y^b \\ \ddot{y}^n = c_\psi \dot{\psi} v_x^b + s_\psi \dot{v}_x^b - s_\psi \dot{\psi} v_y^b + c_\psi \dot{v}_y^b \end{cases}$$

Substituting  $\dot{v}_x^b$  and  $\dot{v}_y^b$  from (2.28), and under the assumption that the blimp moves slowly thus  $m'_x \approx m'_y = m_{\text{Horiz}}$ , it becomes:

$$\begin{cases} \ddot{x}^n = c_\psi \frac{f_{\text{leftxy}} + f_{\text{rightxy}}}{m_{\text{Horiz}}} - s_\psi \frac{f_{\text{leftyz}} - f_{\text{rightyz}}}{m_{\text{Horiz}}} + c_\psi a_x v_x^b - s_\psi a_y v_y^b \\ \ddot{y}^n = s_\psi \frac{f_{\text{leftxy}} + f_{\text{rightxy}}}{m_{\text{Horiz}}} + c_\psi \frac{f_{\text{leftyz}} - f_{\text{rightyz}}}{m_{\text{Horiz}}} + c_\psi a_y v_y^b + s_\psi a_x v_x^b \end{cases}$$

where  $a_x = D_{v_x}/m_{\text{Horiz}}$ ,  $a_y = D_{v_y}/m_{\text{Horiz}}$ . Then from the inverse of kinematic model (2.27), substituting the terms  $v_x^b$  and  $v_y^b$  into  $\dot{x}^n$  and  $\dot{y}^n$ , there is

$$\begin{cases} \ddot{x}^n = c_\psi \frac{f_{\text{leftxy}} + f_{\text{rightxy}}}{m_{\text{Horiz}}} - s_\psi \frac{f_{\text{leftyz}} - f_{\text{rightyz}}}{m_{\text{Horiz}}} + \left( a_x c_\psi^2 + a_y s_\psi^2 \right) \dot{x}^n + (a_x c_\psi s_\psi - a_y c_\psi s_\psi) \dot{y}^n \\ \ddot{y}^n = s_\psi \frac{f_{\text{leftxy}} + f_{\text{rightxy}}}{m_{\text{Horiz}}} + c_\psi \frac{f_{\text{leftyz}} - f_{\text{rightyz}}}{m_{\text{Horiz}}} + \left( a_y c_\psi^2 + a_x s_\psi^2 \right) \dot{y}^n + (a_x c_\psi s_\psi - a_y c_\psi s_\psi) \dot{x}^n \end{cases}$$

For the angular movement, the kinematic relation tells that  $\dot{\psi} = \omega_z^b$ , under the assumption that the blimp moves slowly thus  $m'_x \approx m'_y = m_{\text{Horiz}}$ . Hence the third equation of (2.28) becomes:

$$\ddot{\psi} = \frac{(f_{\text{leftxy}} - f_{\text{rightxy}}) l}{I'_z} + a_\psi \dot{\psi}$$

where  $a_\psi = D_{\omega_z}/I'_z$ .

In summary, we obtain

$$\begin{cases} \ddot{x} = c_\psi \frac{f_{\text{leftxy}} + f_{\text{rightxy}}}{m_{\text{Horiz}}} - s_\psi \frac{f_{\text{leftyz}} - f_{\text{rightyz}}}{m_{\text{Horiz}}} + \left( a_x c_\psi^2 + a_y s_\psi^2 \right) \dot{x} + (a_x c_\psi s_\psi - a_y c_\psi s_\psi) \dot{y} \\ \ddot{y} = s_\psi \frac{f_{\text{leftxy}} + f_{\text{rightxy}}}{m_{\text{Horiz}}} + c_\psi \frac{f_{\text{leftyz}} - f_{\text{rightyz}}}{m_{\text{Horiz}}} + \left( a_y c_\psi^2 + a_x s_\psi^2 \right) \dot{y} + (a_x c_\psi s_\psi - a_y c_\psi s_\psi) \dot{x} \\ \ddot{\psi} = \frac{(f_{\text{leftxy}} - f_{\text{rightxy}})l}{I_z} + a_\psi \dot{\psi} \end{cases}$$

Note that the superscript  $(\cdot)^n$  for  $x$  and  $y$  is omitted for simplicity of notation.

For clarity of the expression, rewrite the blimp simplified planar movement model as:

$$\begin{cases} \ddot{x} = c_\psi b u - s_\psi d w + \kappa_1(a_x, a_y, \psi) \dot{x} + \kappa_3(a_x, a_y, \psi) \dot{y} \\ \ddot{y} = s_\psi b u + c_\psi d w + \kappa_2(a_x, a_y, \psi) \dot{y} + \kappa_3(a_x, a_y, \psi) \dot{x} \\ \ddot{\psi} = b_\psi v + a_\psi \dot{\psi} \end{cases}$$

Let us consider the variables  $u$ ,  $w$ , and  $v$  as the control inputs. These inputs can be expressed as follows:  $u = u_{\text{left}} + u_{\text{right}}$ ,  $w = w_{\text{left}} + w_{\text{right}}$ , and  $v = u_{\text{left}} - u_{\text{right}}$ . Here,  $u_{\text{right}}$  and  $u_{\text{left}}$  represent the command signals for the right and left motors, respectively, while  $w_{\text{right}}$  and  $w_{\text{left}}$  represent the command signals for motors  $M1$  and  $M4$  respectively. The coefficients  $b$ ,  $d$ , and  $b_\psi$  are associated with these control inputs.

The coefficients  $\kappa_1(a_x, a_y, \psi)$ ,  $\kappa_2(a_x, a_y, \psi)$ , and  $\kappa_3(a_x, a_y, \psi)$  are determined by the parameters  $a_x$ ,  $a_y$ , and  $\psi$ . Specifically,  $\kappa_1(a_x, a_y, \psi) = a_x c_\psi^2 + a_y s_\psi^2$ ,  $\kappa_2(a_x, a_y, \psi) = a_y c_\psi^2 + a_x s_\psi^2$ , and  $\kappa_3(a_x, a_y, \psi) = a_x c_\psi s_\psi - a_y c_\psi s_\psi$ .

It is important to note that the command signals  $u_{\text{right}}$ ,  $u_{\text{left}}$ ,  $w_{\text{right}}$ , and  $w_{\text{left}}$  are dimensionless quantities. Therefore, the coefficients  $b$  and  $d$  have the same units as  $\ddot{x}$ , while the parameter  $b_\psi$  has the same unit as  $\ddot{\psi}$ . Additionally, the parameter  $l$ , which represents the half distance between motors  $M2$  and  $M3$ , is incorporated into the parameter  $b_\psi$ .

## 2.4.5 Conclusion

In conclusion, the second chapter provided a comprehensive approach to the dynamic modelling of the system. We started by establishing the assumptions that would guide our modelling process. Following this, we delved into the kinematic and dynamic modelling of the system, providing a detailed analysis of the inertial and body frames, rotational matrix and convention, and the kinematic and dynamic

models themselves.

We then proposed a simplified model, outlining its schematic structure and the assumptions made to simplify the model. This model was further divided into altitude movement and planar movement models, each with their unique characteristics and applications.

## Chapter 3

# Design and Implementation

In this chapter, our focus will be on the design and implementation process that takes us from the dynamic model to the final device. Specifically, we will delve into the study of how the device is capable of adjusting its position based on its pose knowledge. The steps involved in achieving this objective are as follows:

- **Sensors:** The board is equipped with a variety of sensors, each possessing unique characteristics, which will be elaborated upon and seamlessly integrated into the state estimation module.
- **State Estimator:** During this step, the device collects data from various sensors and feeds them into the Kalman estimator. With a certain level of confidence, it can determine its position and attitude.
- **PID Controller:** Once the device has comprehended its position and attitude, it aims to minimize the error between the estimated position and the desired setpoint. The PID controller plays a crucial role in this process.
- **Power Distribution:** The PID controller provides information about a quantity that needs to be converted in order to accurately transmit this information to the motors. This task is carried out by the power distribution block.
- **Propeller linearization and Battery compensation:** The propellers that are usually used in these contests are usually optimized to work just in one direction, so the thrust generated by a motor depends on the propeller and

also on the battery voltage. With this block, we compensate and linearize the behaviour of the motors.

- ESC and Motors: The information from the power distribution stage is then converted into a PWM signal, which is further transformed into a signal capable of driving brushless motors.

Throughout this chapter, we will explore these steps in detail, highlighting the intricacies involved in transitioning from the dynamic model to the functioning device.

## 3.1 Sensors

Let us take a look at the sensors used for the blimp system which provide measurements for state estimation and control process.

The choice of sensors for the blimp robot system depends on various factors, including the desired operations for the robot to achieve, the hardware restrictions (e.g. weight limit, energy limit, installation position and method), etc. Therefore it puts forward specified requirements on the measuring method, precision and measurement frequency of the sensors.

On the other way, the information provided by the sensors also influences the observer and controller design for the blimp system, and leads to the success or failure of the blimp motion control task.

We described in 2.4.1 the dimension of the blimp and its weight. I worth noticing that the 150 grams of payload has to include all the hardwares including gondola structure to fix the micro-controller board to the hull, the motors with propellers as the system actuators, the battery for power supply and wireless communication devices for the possibility of data exchange with host computer. Therefore only low weight sensors and actuators can be integrated in an embedded micro-system, which means the measurement of on-board sensors cannot be very accurate.

After careful consideration, the decision was made to utilize a specially designed board tailored for the application and advancement of nanodrones known as *Crazyflie*. Specifically, the chosen board is the remarkable Crazyflie Bolt board,

renowned for its compatibility with brushless motors. Subsequent chapters will delve into the detailed explanations behind this selection.

### **3.1.1 Crazyflie Bolt**

The Crazyflie Bolt is a quadcopter board developed by Bitcraze, a company with a mission of developing a research-friendly, open-source nano-drone called Crazyflie. The Bolt expands upon the original Crazyflie's capabilities, offering the possibility to attach brushless motors and develop your own robot. It is designed to be hackable, making it an ideal tool for developers, researchers, or anyone interested in the field of drone technology.

The Crazyflie Bolt is packed with sensors that make it an ideal platform for development and experimentation. Here are the key sensors found in the Crazyflie Bolt:

- **Inertial Measurement Unit(IMU):** The primary sensor in the Crazyflie Bolt is the Bosch BMI088, a high-performance 6DoF IMU (Inertial Measurement Unit). This includes a 3-axis accelerometer and a 3-axis gyroscope, which allow the drone to sense its acceleration and rotational speed.
- **Pressure Sensor:** The drone also contains a Bosch BMP388 pressure sensor, which measures atmospheric pressure. This can be used to estimate altitude, a critical parameter for drones.
- **Expansion Ports:** The Crazyflie Bolt is designed to be highly expandable, with several expansion ports that allow the addition of other plug and play, and possible-to-buy, sensors and modules. This can include GPS modules, additional cameras, ultrasonic sensors for distance measurement, optical flow sensors for improved stability and position tracking, or any other sensor that the user needs for their specific application.
- **Radio:** The Crazyflie Bolt is equipped with a nRF24LU1+ 2.4 GHz radio transceiver for communication. This can be used for real-time control, telemetry, and even software updates.

- **Power Management:** The Crazyflie Bolt is equipped with a power management system that includes battery voltage and current monitoring. This can be critical for understanding the drone's flight time and battery health.

These sensors, coupled with the powerful STM32F405 microcontroller and the open-source firmware, make the Crazyflie Bolt a versatile tool for research and development in the field of drone technology. It's possible to implement a variety of control algorithms, from simple stabilization to complex path planning and tracking. The ability to access raw sensor data, as well as processed state estimates, make it a powerful platform for experimentation and learning.

The Crazyflie Bolt can be expanded by attaching a board called Flowdeck V2 to it. This deck is essentially a sensor module that enhances the capability of the drone by adding a way to measure distances and detect movements relative to the ground. Here are the primary components of the Flow deck v2:

- **Optical Flow Sensor (PMW3901):** The primary component of the Flow deck is an optical flow sensor. It works similarly to an optical mouse, tracking the movement of the drone relative to the ground. This sensor measures the motion of the drone by continuously taking images of the ground and comparing them. This way, it can calculate how fast and in what direction the drone is moving horizontally, which is particularly useful for indoor navigation.
- **Time-of-Flight Distance Sensor (VL53L1x):** Also included in the Flow deck v2 is a Time-of-Flight (ToF) distance sensor. This sensor works by emitting a light signal and then measuring the time it takes for the light to bounce back, hence the name "time-of-flight". By knowing the speed of light, it can calculate the distance to the object. This sensor can be used to measure the height of the drone above the ground, which is useful for maintaining a steady altitude.

The combination of the optical flow and ToF sensors allows for a degree of autonomous flight, even in environments without GPS. This is particularly useful in indoor or urban environments where GPS signals can be weak or non-existent. The drone can maintain a stable hover by using the ToF sensor to hold altitude and the optical flow sensor to hold the position.

The Flow deck v2 is mounted on the expansion port of the Crazyflie Bolt, which provides power and a data connection. The sensor data is processed by Crazyflie's onboard microcontroller and can be used in the control algorithm. This, combined with Bolt's existing sensors and the open-source firmware, makes it a powerful tool for research and development in the field of drone technology.

### **3.1.2 Motion Capture System**

After conducting initial trials on the blimp prototype and summarizing the gathered experiences, a decision has been made to incorporate a camera-capturing system called Qualysis in the testing room. This system aims to track the robot's movements and acquire precise measurements of its position and orientation. The Qualysis system utilizes infrared waves to detect the reflective markers placed on the blimp's hull. By analyzing these markers, it determines the robot's pose at a remarkable rate of 100 frames per second. The system boasts an impressive positional measurement precision of 1 mm.

A visual representation of the Qualisys system is shown in Figure 3.1. The camera capturing system does more than just sense the environment—it performs image processing and estimates the 'pose', a term used to describe the combined localization and orientation of the blimp. Once the pose is determined, the system relays the results to the blimp control system. Given the nature of the blimp's operation, it's plausible that the Qualisys system could serve as the sole sensor, providing all the necessary pose data for the blimp's navigation and control.

One of the notable advantages of employing the camera-capturing system is its ability to provide highly accurate localization data and orientation measurements for the robot. These measurements remain stable over time, unaffected by drifting issues. Furthermore, the system's frequency is sufficiently high to accommodate even vigorous robot movements.

While there are certain limitations associated with our current approach, they are outweighed by the benefits it provides. The camera capturing system, although fixed within the testing room's environment, offers precise localization within this area. This limitation on autonomy is a trade-off we accepted in order to focus on the primary objective of this project: blimp motion control.

The cost of the system, while significant, is justified by the quality of the results

it delivers. It's important to note that our choice to use the Qualisys system was strategic. It provides high-quality ground-truth measurements, which are crucial for the accurate parameter identification of the blimp under investigation.

While we acknowledge the challenges of autonomous localization and navigation in unfamiliar environments, these are areas for future exploration. We are confident that, if required, we could have made OpticalFlow work, demonstrating our team's adaptability and problem-solving capabilities. For the scope of this project, however, the Qualisys system was the most suitable choice.

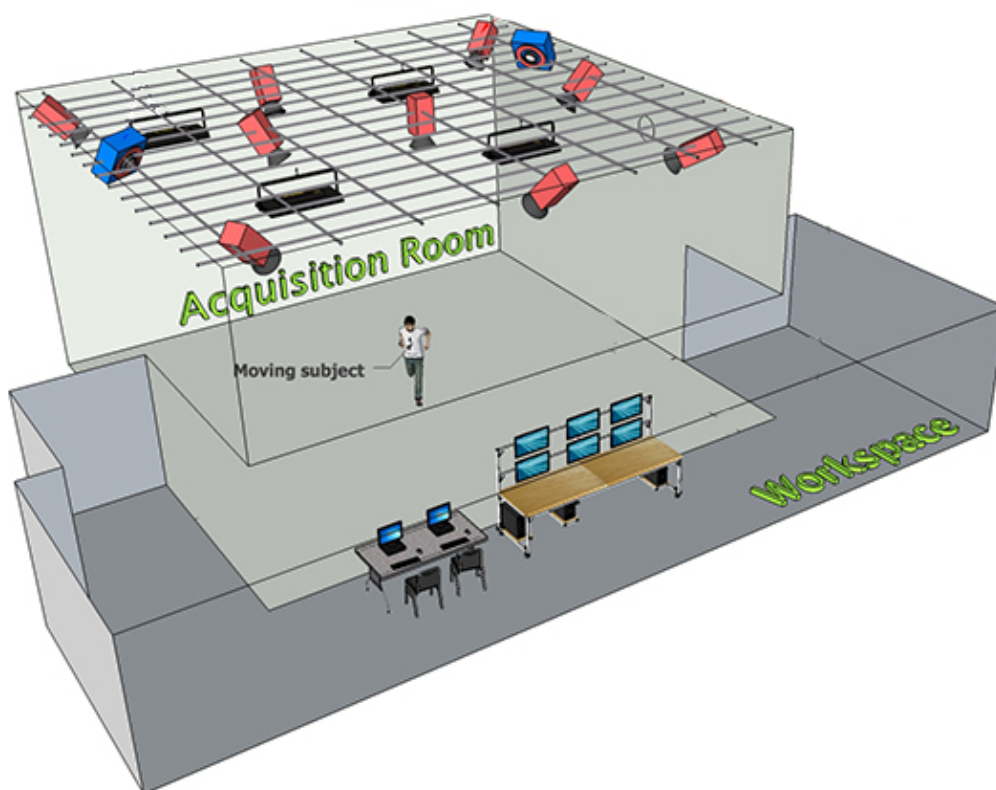


**Figure 3.1:** Description of the motion capture system Qualisys

## 3.2 State Estimation with Kalman Filter

The state estimation process plays a crucial role in the control and navigation of the miniature indoor blimp. In this section, we will provide a brief explanation of

the mathematical model used in the state estimation algorithm, specifically the Kalman filter. It is important to note that the firmware used for the Crazyflie board already incorporates the Kalman filter; therefore, our focus was primarily on providing accurate measurements together with standard deviation from the Qualisys system.

The Kalman filter is an optimal recursive estimator that utilizes a system's dynamic model and noisy measurements to estimate the true state of the system. It operates in two main steps: the prediction step and the update step.

### 3.2.1 Prediction Step

In the prediction step, the Kalman filter predicts the current state of the system based on the previous state estimation. This prediction is obtained by applying the system's dynamic model. Let  $\mathbf{x}_k$  represent the state vector at time step  $k$ . The prediction equation can be expressed as:

$$\hat{\mathbf{x}}_k^- = \mathbf{F}_k \hat{\mathbf{x}}_{k-1}$$

where  $\mathbf{F}_k$  is the state transition matrix that relates the current state to the previous state.

The predicted state estimation error covariance, denoted as  $\mathbf{P}_k^-$ , is also updated based on the dynamic model:

$$\mathbf{P}_k^- = \mathbf{F}_k \mathbf{P}_{k-1} \mathbf{F}_k^T + \mathbf{Q}_k$$

where  $\mathbf{Q}_k$  represents the process noise covariance.

### 3.2.2 Update Step

The update step incorporates the measurements obtained from the sensors to refine the state estimation. The Kalman filter computes the Kalman gain, which determines the optimal balance between the predicted state and the measurements. Let  $\mathbf{z}_k$  denote the measurement vector at time step  $k$ .

The Kalman gain, denoted as  $\mathbf{K}_k$ , is calculated as follows:

$$\mathbf{K}_k = \frac{\mathbf{P}_k^- \mathbf{H}_k^T}{\mathbf{H}_k \mathbf{P}_k^- \mathbf{H}_k^T + \mathbf{R}_k}$$

where  $\mathbf{H}_k$  is the measurement matrix that maps the predicted state to the measurement space, and  $\mathbf{R}_k$  represents the measurement noise covariance.

Using the Kalman gain, the update equation for the state estimation is given by:

$$\hat{\mathbf{x}}_k = \hat{\mathbf{x}}_k^- + \mathbf{K}_k(\mathbf{z}_k - \mathbf{H}_k \hat{\mathbf{x}}_k^-)$$

Finally, the updated state estimation error covariance, denoted as  $\mathbf{P}_k$ , is computed as:

$$\mathbf{P}_k = (\mathbf{I} - \mathbf{K}_k \mathbf{H}_k) \mathbf{P}_k^-$$

where  $\mathbf{I}$  is the identity matrix.

### 3.2.3 Final Process

In the prediction step, the Kalman filter projects forward the current state and error covariance estimates to obtain the a priori estimates for the next time step. This step incorporates the system dynamics and control inputs, providing an initial estimate of the state.

The update step follows the prediction. Here, the Kalman filter refines the predicted estimates using the new measurements. The difference between the actual measurement and the predicted state, known as the measurement residual, is used to correct the prediction. The state covariance is also updated, reducing the uncertainty in the state estimate.

These two steps work in tandem, continuously predicting and correcting the state estimate. The prediction step provides an initial estimate, and the update step refines this estimate based on new measurements. This balance between prediction and correction allows the Kalman estimator to effectively handle noise in the measurements and uncertainties in the system dynamics.

In conclusion, the Kalman estimator serves as a powerful tool for state estimation in dynamic systems. By iteratively predicting and updating the state estimates, it

provides an optimal balance between system dynamics and actual measurements, resulting in an accurate and reliable state estimate.

### **3.2.4 Work Done**

In this research, the firmware used for the Crazyflie board already includes the Kalman filter, which is essential for estimating the state of the system by utilizing all the sensors on the board. This step is particularly important for the future implementation of an indoor blimp that doesn't rely on a motion capture system. Our main contribution in this aspect was providing accurate standard deviations for the measurements obtained from the Qualisys system. Through careful calibration of the Qualisys system and analysis of the data, we were able to estimate the correct standard deviations for each measurement variable, including position, velocity, and orientation. This information was crucial for the precise control and navigation of the miniature indoor blimp, as it allowed the Kalman filter to effectively combine the sensor measurements and provide reliable state estimates.

By incorporating the correct standard deviations of the Qualisys measurements into the state estimation algorithm, we improved the overall performance and accuracy of the miniature indoor blimp. Additionally, this work enhanced the reliability and robustness of the system, enabling it to navigate indoor environments effectively and fulfill its intended tasks.

## **3.3 PID Controller**

The PID (Proportional-Integral-Derivative) controller is a fundamental control algorithm widely used in various systems, including the control of unmanned aerial vehicles (UAVs). In this section, we will introduce the PID controller and its role in achieving precise spatial position control of the miniature indoor blimp. The development and tuning of the PID controller were essential steps in ensuring stable and responsive control of the blimp's movements.

The PID controller operates by continuously calculating an output control signal based on the error between the desired setpoint and the current state of the system. It combines three control components: proportional, integral, and derivative, each

contributing to different aspects of the control behavior.

The proportional component generates an output proportional to the current error. It provides a direct response to the present error and contributes to the overall system stability and steady-state error reduction. The integral component integrates the accumulated error over time, compensating for any steady-state errors and enhancing the system's ability to track the setpoint accurately. The derivative component anticipates the future error trend based on the rate of change of the error. It helps dampen the system's response and improve its transient behavior.

The PID controller is characterized by three tunable parameters: the proportional gain ( $K_p$ ), integral gain ( $K_i$ ), and derivative gain ( $K_d$ ). The process of tuning these parameters involves finding the appropriate values to optimize the control performance, ensuring stability, responsiveness, and robustness.

In the context of the miniature indoor blimp, we carefully designed and implemented a PID controller to achieve precise spatial position control. Through iterative testing and fine-tuning, we determined the optimal values of  $K_p$ ,  $K_i$ , and  $K_d$  to achieve stable and accurate control of the blimp's movements. The PID controller was integrated with the state estimator to provide accurate feedback for control actions, enabling the blimp to maintain its position and respond to changes in setpoints effectively.

The implementation of the PID controller significantly contributed to the overall control performance of the miniature indoor blimp. It allowed for precise and responsive control, enabling the blimp to hover, move, and follow desired trajectories with high accuracy. The development and tuning of the PID controller played a vital role in realizing the objectives of this research and establishing the blimp as a capable indoor exploration and surveillance vehicle.

In the following sections, we will delve into the design considerations, tuning process, and performance evaluation of the PID controller for the miniature indoor blimp, providing insights into its effectiveness and the achieved control capabilities.

### **3.3.1 Controller Design Considerations**

Based on the information provided in the preceding section and taking into account our previous deliberations, it is evident that our airship possesses the capability to

maneuver across the three Cartesian axes. Additionally, it can execute a rotational movement along the  $Z_b$  axis, known as yaw motion. With this understanding, we can determine that employing four sets of PID controllers is necessary to minimize the error associated with each variable.

The PID controller we have chosen to implement comprises an outer loop, responsible for regulating position errors, and an inner loop, which focuses on controlling velocity during linear movements. In the case of yaw motion, the underlying principle remains the same, although the terminology differs, referring to attitude and rate instead.

The reason for using a velocity loop inside a position loop (commonly known as a cascaded PID controller) when controlling a quadcopter is due to the dynamics of the system and the need to ensure stability and responsiveness of control. The velocity controller can react faster than the position controller, providing stability and control precision.

The already implemented PID controller in the Crazyflie firmware has the structure described in Fig.3.2.

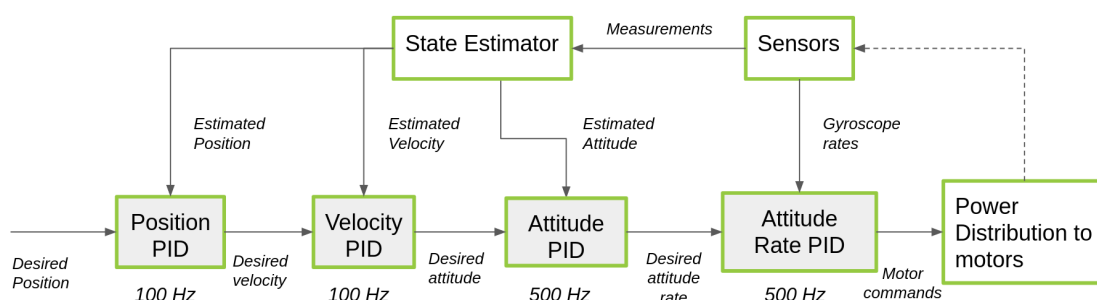


**Figure 3.2:** Cascaded PID Controller schematization in the crazyflie firmware [Source:<https://www.bitcraze.io/documentation/repository/crazyflie-firmware/master/functional-areas/sensor-to-control/controllers/cascaded-pid-controller>]

Utilizing the state estimation and the information regarding the desired position, the error is fed into a position controller. This controller then provides the target velocity to be fed into a velocity controller. For the case of quadcopter, the movement along the plane denoted as  $OXY$  is achieved through a combination of pitch and roll movements. The pitch movement corresponds to a rotation

around the X-axis, while the roll movement corresponds to a rotation around the Y-axis. These attitude changes are necessary to redirect the thrust produced by the propellers in the desired direction.

At this point, it is important to note that the movement of the blimp is not influenced by roll and pitch, but rather by motor displacement. The dynamics of the blimp are designed in a manner where such movements are directly proportional to its motion. By adjusting the speed or rotation of the motors, the blimp can move in the desired direction. Unlike a quadcopter, which relies on changes in roll and pitch to control its movement along the X and Y axes, the blimp's dynamics allow for direct translation without the need for attitude adjustments.

One aspect of our task involved altering the framework of the previously employed PID Controller to align it with our specific requirements. The image depicted in Figure 3.3 showcases these modifications that were made.

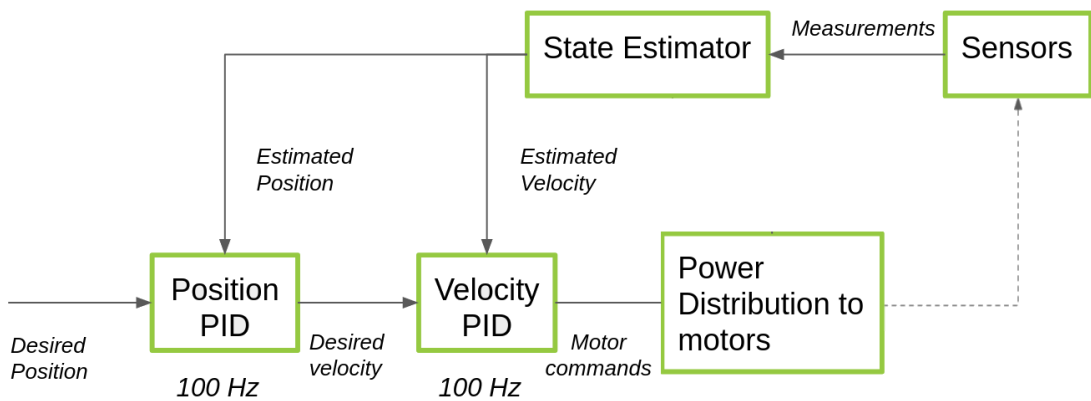


**Figure 3.3:** Schematization of the PID Controlled used for the blimp

The Tuning Process of the PID Controlled will be described in the next chapter.

### 3.4 Power Distribution

The power distribution block in the firmware plays a crucial role in translating the output of the PID Controller into motor commands that align with the desired movement of the blimp. It acts as a communication interface between the PID controller and the electronic speed controllers (ESCs) responsible for driving the

motors.

To effectively control the movement of the blimp, the output signals from the PID controller need to be appropriately scaled and translated into motor commands that align with the desired motion. The power distribution block serves as an intermediary, ensuring that the control signals from the PID controller are processed and delivered to the ESCs in a coherent and synchronized manner. This involves mapping the control signals to appropriate ranges and ensuring that they are within the operational limits of the motors and ESCs.

Additionally, the power distribution block translates the control commands into signals that are compatible with the ESCs. These signals typically involve pulse-width modulation (PWM) techniques, where the duration of the pulse determines the motor speed or rotation. The power distribution block ensures that the PWM signals are generated accurately, synchronized, and transmitted to the ESCs, enabling precise control of each motor's speed and direction.

Furthermore, the power distribution block ensures the synchronization and coordination of motor commands. As the blimp may require coordinated movements between different motors, the power distribution block handles the timing and sequencing of motor activations and adjustments. This coordination is essential for maintaining stability, balance, and accurate control of the blimp's movement.

By effectively managing the communication and coordination between the PID controller and the motors, the power distribution block plays a critical role in maneuvering the blimp. Its precise control over the motor commands enables the blimp to accurately navigate and maintain its position within the desired trajectory.

In the subsequent sections, we will delve deeper into the specific mechanisms and algorithms employed in the power distribution block, highlighting its importance in achieving controlled and stable movements of the miniature indoor blimp.

### 3.4.1 Output of the Controller and scaling

As we have seen the PID Controller generates an output representing the velocity that the blimp has to have to reach the desired position. The PID implemented in the firmware of the used board is such that the output is a *float* variable that has a span of value that goes from  $-20$  to  $+20$ . The power distribution block is able to work with unsigned integer values that go from 0 to 65535. These values are

then passed to another function that is able to generate the PWM signal in the Oneshot125 protocol.

The operation of the power distribution block begins with understanding the output from the Proportional-Integral-Derivative (PID) controller. This controller is designed to produce an output corresponding to the necessary velocity for the blimp to reach its target position. In the firmware of the utilized board, this output is implemented as a floating-point number, denoted as  $v_{PID}$ , within the range  $[-20, 20]$ .

However, the power distribution block necessitates unsigned integer values for its operation. These integer values, denoted as  $p_{DB}$ , lie within the range  $[0, 65535]$ . Following this, they are used by a function dedicated to generating a Pulse-Width Modulation (PWM) signal in accordance with the Oneshot125 protocol.

$$p_{DB} : \mathbb{Z} \rightarrow [0, 65535]$$

It's worth noting that in the firmware, 0 and 65535 correspond to the motor being turned off and operating at full speed, respectively. However, this mapping does not cater to our requirement for bidirectional control over the motors. Consequently, we require a remapping of these values to ensure that the mid-range corresponds to the motor being stationary, while values above and below this midpoint correspond to the motor spinning in opposite directions.

We define a midpoint value  $p_{mid} = 32768$ . In our scenario, we want this midpoint to correspond to the motor being stationary, i.e.,  $v_{PID} = 0$ , and values above and below this midpoint should correspond to the motor spinning in opposite directions, i.e.,  $v_{PID} > 0$  and  $v_{PID} < 0$  respectively.

The mapping function  $f$  can be defined as follows:

$$f(v_{PID}) = \frac{v_{PID}}{40} \cdot 65535 + p_{mid}$$

such that  $f(-20) = 0$  and  $f(20) = 65535$ .

These commands need to be sent to the output of the board to which the motors are connected. However, as they are currently formulated, these commands do not provide accurate information regarding which motor needs to spin in order to execute these movements.

Considering the motor nomenclature as illustrated in Fig. 2.2, it can be observed that to achieve movement along the  $X_b$ -axis, motors  $M_2$  and  $M_3$  need to spin in the same direction. It is assumed that when the same command is given, these two motors spin in opposite directions to prevent the generation of moments that could lead to further rotation along the  $X_b$ -axis while producing thrust in the desired direction. These two motors are also employed to control yaw rotation by generating counteracting forces. The two bottom motors,  $M_1$  and  $M_4$ , are utilized for movement along the  $Z_b$ -axis, enabling the blimp to attain and maintain the correct altitude. Additionally, these two motors are involved in generating movement along the  $Y_b$ -axis through counter-rotation.

The commands given to the motors are modeled as follows:

$$\begin{aligned}
 M_2 &= \frac{v_{xPID}}{2} + \frac{\omega_{zPID}}{2} \\
 M_3 &= \frac{v_{xPID}}{2} - \frac{\omega_{zPID}}{2} \\
 M_1 &= \frac{v_{zPID}}{2} + \frac{v_{yPID}}{2} \\
 M_4 &= \frac{v_{zPID}}{2} - \frac{v_{yPID}}{2}
 \end{aligned} \tag{3.1}$$

Finally, the Electronic Speed Controller (ESC) firmware also needs to interpret the PWM signal correctly to induce the desired motor behaviour. The mapping function will need to be reversed in the ESC firmware to interpret the received  $p_{DB}$  value correctly and induce the corresponding motor behaviour.

### 3.5 Propeller Analysis, Linearization, and Battery Compensation

In this section, we turn our attention towards a crucial element in the overall performance of our indoor blimp: the propeller. Propeller selection is a key step in the design process of any Unmanned Aerial Vehicle (UAV), as it significantly influences the dynamics, motion, and power consumption of the device under study. As such, an in-depth analysis of the propeller is instrumental in enhancing the efficiency and stability of our indoor blimp.

Initially, we examine various propellers, considering their generated thrust and

current draw. This rigorous comparative study aims to identify the propeller that can provide an optimal balance between thrust generation and energy consumption, thereby maximising the performance of the blimp.

Post selection, our focus shifts to refining the performance of the chosen propeller. Here, we introduce a method to linearize the propeller's behavior across the full range of values that allow the motor to spin at different speeds. Linearization of the propeller's performance ensures a predictable and controlled response from the motor, further increasing the device's stability and manoeuvrability.

Lastly, to augment the efficiency of the PID Controller and enhance the overall stability of the blimp, we introduce a battery compensation algorithm. As the battery discharges over time, the voltage supplied decreases, causing a corresponding decrease in the thrust generated by the motor. Our battery compensation algorithm counters this effect, ensuring a consistent motor thrust irrespective of the battery's charge state.

Through this in-depth examination and fine-tuning of the propeller and associated factors, we strive to create a robust, reliable, and high-performing indoor blimp that operates efficiently even as the battery discharges.

### **3.5.1 Propeller Analysis**

Propellers play an important role in defining the flight characteristics of Unmanned Aerial Vehicles (UAVs). Their attributes significantly impact the UAV's dynamic behavior, energy consumption, and manoeuvrability, making a comprehensive analysis of different propeller characteristics essential.

Propellers primarily vary based on their dimension, number of blades, and shape.

- **Dimension:** The size of the propeller crucially determines the thrust generated. Larger propellers displace a greater volume of air, thereby producing increased thrust. However, these propellers demand more power to operate, potentially leading to higher energy consumption [6]. While larger propellers may improve performance concerning thrust and lift, their efficacy may be compromised in micro UAVs due to the escalated power demand.
- **Number of blades:** Propellers can sport anywhere between two to six blades. Although increasing the number of blades can generate more thrust, it

simultaneously increases the power requirement. More blades may also reduce the propeller's efficiency and amplify the noise for a given thrust[7].

- **Shape:** The form of a propeller significantly influences its performance. Factors such as the curvature, pitch, and aspect ratio of the propeller blades determine how effectively the propeller cuts through the air, affecting the generated thrust[8].

In addition to these primary attributes, several other factors can impact the effectiveness of a propeller. These include the propeller material, pitch angle, blade airfoil, and RPM limits.

- **Material:** Propellers can be crafted from a variety of materials, including plastic, carbon fiber, and wood. The choice of material influences the propeller's durability, weight, and cost [9].
- **Pitch:** The pitch of a propeller, typically measured in inches, represents the distance that a propeller would move forward in one revolution if it were moving through a soft solid. Propellers with a higher pitch displace more air, thereby generating more thrust, but also require more power to operate.
- **Blade Airfoil:** The airfoil shape of the blade affects the lift-to-drag ratio, which, in turn, determines the efficiency and performance of the propeller[10].
- **RPM limits:** Each propeller comes with a recommended RPM (Revolutions Per Minute) limit. Exceeding these limits can lead to reduced efficiency, increased noise, and potential mechanical failure.

This research focuses on the use of a lightweight structure for our blimp, and therefore, careful consideration was given to the selection of propellers. The choice was narrowed down to four different commercially available propellers, differentiated by their shape, blade count, and size. The primary objective of this analysis was to optimize the efficiency of our airborne device. The selected propellers are illustrated in Fig. 3.4.

The measurement setup used for propeller analysis employed a precision scale and a bench power supply, allowing us to monitor the current draw under fixed



**Figure 3.4:** Studied propellers (from left to right): 2-Blade 40mm, Smooth 4-Blade 40mm, Rigid 4-Blade 40mm, 3-Blade 31mm.

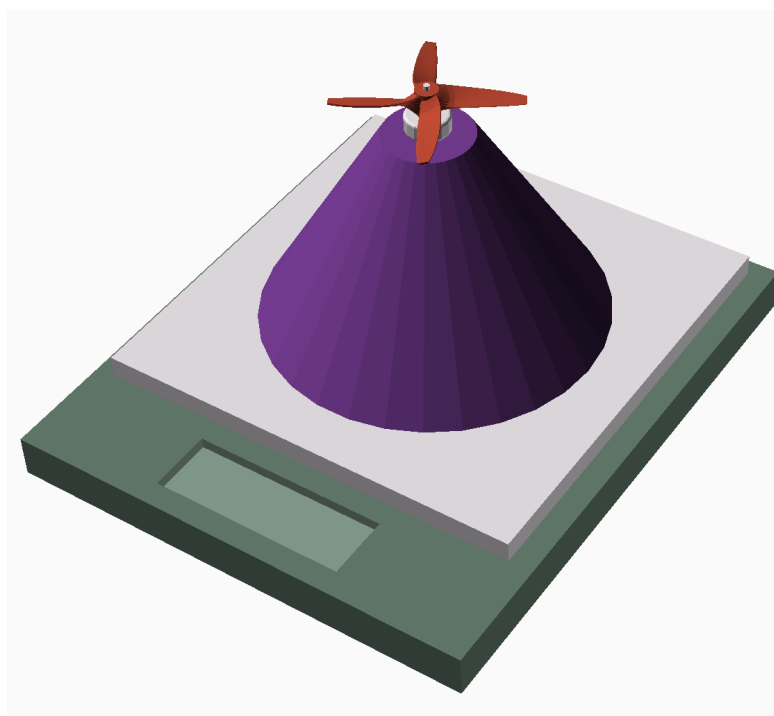
applied voltage ( $V_{ps} = 4.0V$ ), while simultaneously measuring the thrust generated by the propeller-attached motor. The command input provided to the controller corresponds to a value within the range  $[0, 65535]$ .

Fig. 3.5 shows the experimental setup. The motor, along with its attached propeller, is mounted on a structure placed on a precision scale. The thrust generated by the motor is indirectly measured as a change in weight recorded by the scale.

The ground effect is a phenomenon that occurs when an aircraft or UAV operates close to the ground. It can cause an increase in lift and a decrease in drag, skewing the true performance measurements of the propellers. To mitigate this, the measurements in our study were taken in two distinct steps, ensuring that the force was always directed towards the precision scale. This methodology aids in obtaining accurate readings of the propellers' performance, free from the potential distortions caused by the ground effect. This two-step process is critical in ensuring the reliability of our findings and the ultimate efficiency of the blimp design.

Figure 3.6 illustrates the relationship between the applied command and the thrust generated by different propellers. Initial observations from these curves affirm the anticipated characteristics of propellers.

Specifically, we observe that propellers with smaller diameters generate less thrust, confirming our earlier understanding of propeller dynamics. Similarly, as the blade count increases, the thrust generation also sees an increase. This underscores



**Figure 3.5:** Measurement setup: A precision scale is positioned beneath a structure to which the propeller-attached motor is mounted. The generated thrust is inferred from the change in recorded weight.

the role of the blade count in influencing the propeller’s performance. Lastly, the shape of the propeller significantly affects thrust generation: a more aggressive propeller shape leads to greater thrust.

These observations validate our foundational understanding of propeller characteristics and provide important insights to inform the optimization of our blimp design.

While the measurements of thrust generation are crucial, they do not present a complete picture for our purpose. To optimize the design of our blimp, we aim to minimize power consumption while preserving satisfactory performance. To that end, we have crafted another plot (shown in fig 3.7) that describes the current draw as a function of generated thrust.

From this plot, we can again confirm the anticipated characteristics of propellers. Larger dimensions and an increased number of blades result in greater torque required to rotate the propeller, leading to higher power consumption. By analyzing

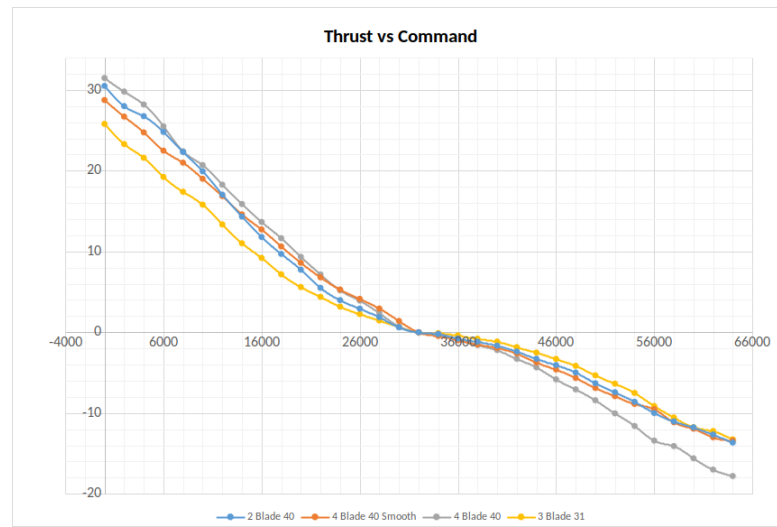


**Figure 3.6:** Thrust generated by different propellers as a function of applied command. On the Y-axis there is the Thrust[g], on the X-axis there is the Command

the ratio between the generated thrust and the current draw, we identify the 2-blade propeller as the most energy-efficient.

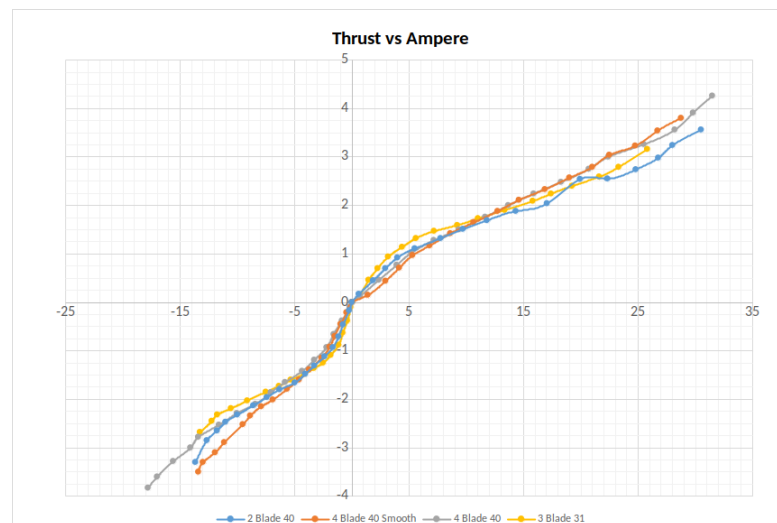


**Figure 3.7:** Current draw by different propellers as a function of generated thrust. On the Y-axis, there is the current draw [A]; on the X-axis, there is the generated thrust [g].

An essential characteristic observable in these graphs is the non-linearity of the

thrust generation curves. The propeller and motor generate thrust that varies depending on the applied command. This characteristic could be attributable to the inherent features of the motor and the electronic speed controller (ESC), as the curve shape appears to be independent of the propeller type. What is directly associated with the propeller, however, is the variation in maximum thrust generated in one direction over the other.

These propellers are designed for nano-quadcopters, which traditionally use motors that spin in one direction, optimizing the propellers to generate thrust specifically in that direction. This design aspect is not suitable for our application. Given that there are currently no commercially available symmetrical propellers, we opted to develop a compensation algorithm to linearize this characteristic. Future work may include designing specialized propellers that suit this characteristic, while also focusing on reducing the dimensions and blade count to further enhance efficiency.

### **3.5.2 Battery Compensation and Linearization**

Developing an effective solution for managing the impacts of battery discharge is of paramount importance in a low-voltage brushless motor system like our blimp. Lithium polymer (Li-Po) batteries, despite their efficiency, have a fluctuating operational voltage range from  $4.2V$  down to  $3.3V$ , even though their nominal voltage is  $3.7V$ . This means the motor speed, and consequently, the overall performance of the system is affected by any battery voltage fluctuation due to the non-ideal characteristics of the components.

Maintaining stability in a complex system such as a blimp becomes a significant challenge considering these factors. The Proportional-Integral-Derivative (PID) Controller, which already compensates for variables like inertia and noise, is further burdened by changes in motor speed caused by battery discharge. This can greatly undermine the blimp's performance and stability, necessitating the development of effective strategies to mitigate these concerns.

Our solution to this issue involved a detailed study of the motor's behaviour under varying voltage conditions. The already used measurement setup with the motor and propeller attached to a precision scale is been modified to use the controller board and attached battery as the power supply. This allowed us to

closely observe how the thrust changes under battery load and as it discharges.

To ensure accurate data collection, we developed a Python script. Initially, the script randomly sends a command ranging from 0 to 32768 to start the motor spinning. Once the motor is spinning, the script retrieves the current battery voltage from the controller board. To measure thrust accurately, we positioned a camera to capture the precision scale's display. An Optical Character Recognition (OCR) algorithm is then used to convert the camera-captured images into numerical data representing the generated thrust. To stop the motor, the script sends the command 32768, capturing the voltage and thrust at rest.

Considering the direction of the propeller's spin in our measurements was a crucial factor. We ensured that our data reflected the motor's operational range by storing the value of the command when the propeller spun in a direction with command values from 32768 to 65535.

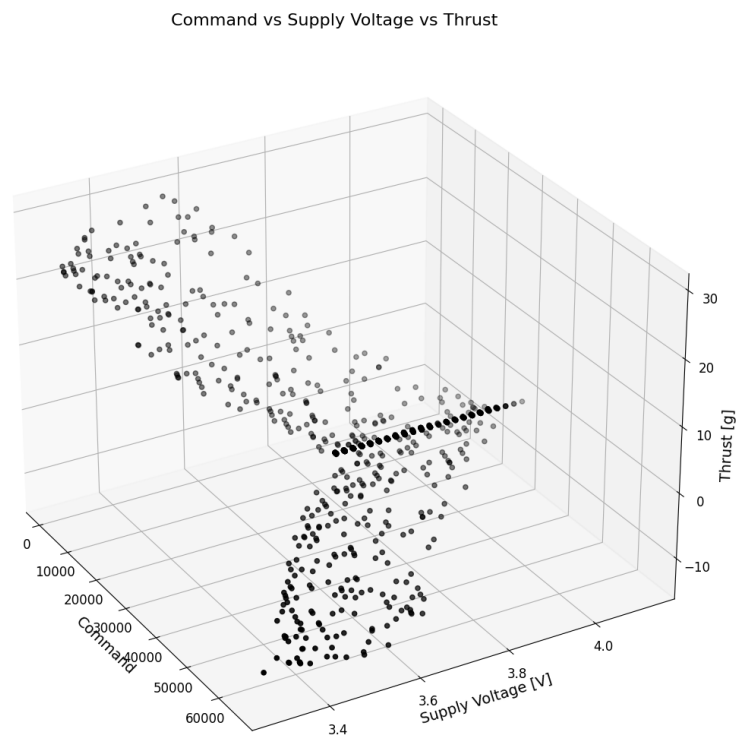


**Figure 3.8:** A 3D scatter plot depicting the system's behaviour as a function of the command and voltage. This plot offers an overall view demonstrating the interaction between variables.

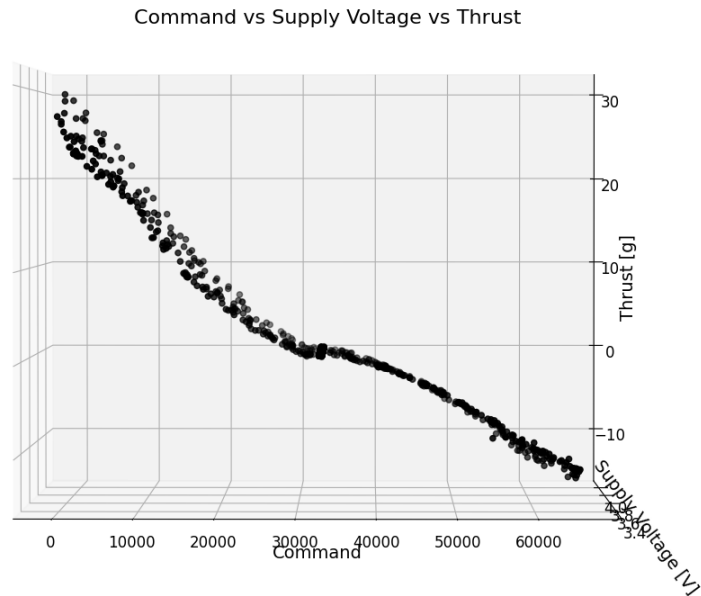


**Figure 3.9:** An alternate view of the 3D scatter plot, focusing on the Command-Thrust plane, which validates our previous propeller analysis measurements.

### Data Visualization and Regression Analysis

After compiling this data, we collected approximately a thousand data points describing the thrust as a function of the command and voltage. This allowed us to create a comprehensive 3D scatter plot that provides insights into the system’s behaviour under various conditions.

These plots, as depicted in Figures 3.8 and 3.9, visually confirm our measurements and theoretical expectations. Through regression analysis, we derived an approximation function that describes the motor’s behaviour across different battery voltages. By incorporating this function into the firmware through hard coding, we developed a means to compensate for battery discharge. The accuracy of this function, combined with continuous voltage readings from the board’s internal voltage sensor, provides a consistent method to compensate for changes in battery voltage, thereby enhancing the overall system performance.

In addition to these plots, we created two more visualizations to represent the thrust as a function of voltage and command but separated by the direction of the motor's spin. These two plots allowed us to reduce the complexity of the regression model by treating each direction as a separate function.

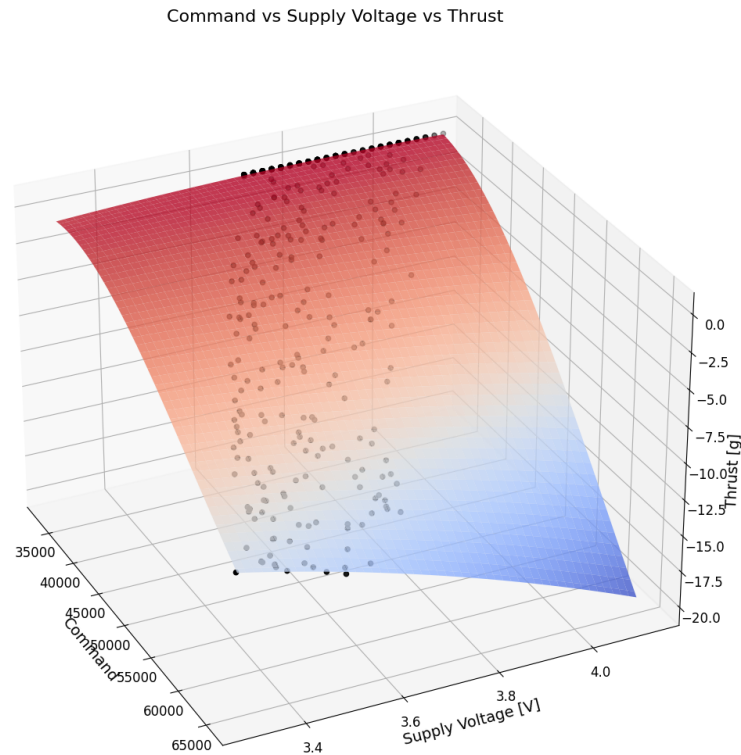


**Figure 3.10:** The 3D scatter plot of the back spinning direction, with a surface plot of the regression result superimposed.

Using these separated scatter plots (Figs. 3.10-3.11, we performed a polynomial regression of the third degree, seeking to approximate the system's behaviour as accurately as possible. We also used a cross-validation process to refine our model and ascertain the best fit for our data.

### Polynomial Regression

In the context of our work, polynomial regression was a fitting choice due to the clear non-linear relationship between our variables: command, voltage, and thrust.

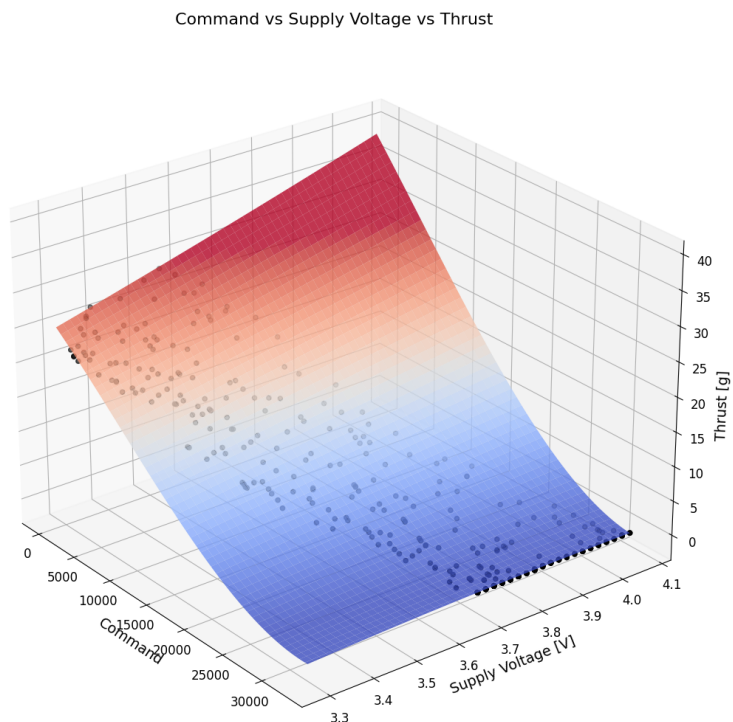


**Figure 3.11:** The 3D scatter plot of the forward spinning direction, with a surface plot of the regression result superimposed.

The third-degree polynomial regression allows us to generate a surface that closely fits the observed data points. This mathematical tool is widely used in machine learning and data analysis for its flexibility and adaptability in modeling complex, non-linear systems.

The objective of polynomial regression is to find an equation of the polynomial of degree  $n$  that best fits the data. In our case, the degree is 3. The model equation for the two directions of spin are as follows.

Let:

- T1 and T2 represent  $Thrust_{dir1}$  and  $Thrust_{dir2}$  respectively,
- V represent Voltage,
- C represent Command,
- $\beta_i$  and  $\beta'_i$  (where  $i$  ranges from 0 to 9) represent the coefficients.

For the first direction of spin:

$$T1 = \beta_0 + \beta_1 \cdot V + \beta_2 \cdot C + \beta_3 \cdot V^2 + \beta_4 \cdot C^2 + \beta_5 \cdot V \cdot C \\ + \beta_6 \cdot V^2 \cdot C + \beta_7 \cdot V \cdot C^2 + \beta_8 \cdot V^3 + \beta_9 \cdot C^3$$

For the second direction of spin:

$$T2 = \beta'_0 + \beta'_1 \cdot V + \beta'_2 \cdot C + \beta'_3 \cdot V^2 + \beta'_4 \cdot C^2 + \beta'_5 \cdot V \cdot C \\ + \beta'_6 \cdot V^2 \cdot C + \beta'_7 \cdot V \cdot C^2 + \beta'_8 \cdot V^3 + \beta'_9 \cdot C^3$$

## **Results and Performance of the Compensation Algorithm**

Evaluating the effectiveness of our compensation algorithm required a comparative analysis under two conditions: fixed command operation with and without the algorithm in place.

In our initial setup, the propeller was set to generate 10 g of thrust with a fixed command of 18000 when the battery was fully charged at 4.2 V. However, without the battery compensation algorithm, the thrust output significantly decreased as the battery voltage dropped. Our measurements, depicted in Figure 3.12, show that the thrust fell from the initial 10 g to about 5 g as the battery discharged.

With our battery compensation algorithm in place, the story was markedly different. When we repeated the experiment, the algorithm dynamically adjusted the command values to maintain near-constant thrust despite the battery's decreasing voltage. As shown in Figure 3.13, the thrust only decreased from 10 g to 9.5 g as the battery discharged, representing a significant improvement in system performance.

An additional plot, illustrated in Figure 3.14, shows the changes in the command value required to maintain this near-constant thrust as the battery discharges. It provides a clear representation of how the compensation algorithm dynamically adjusts the command values to ensure consistent performance, thereby significantly mitigating the impacts of battery discharge.

Beyond battery compensation, our algorithm also tackled the propeller's non-linear behaviour. To demonstrate the effectiveness of this aspect of our solution, we

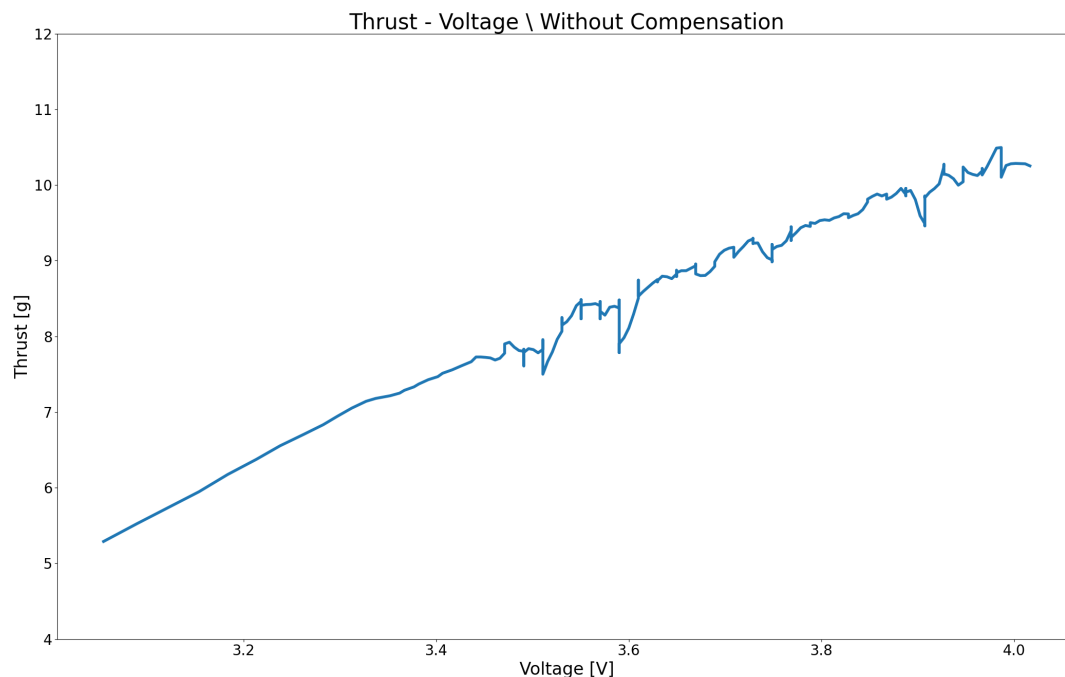


**Figure 3.12:** Thrust output as a function of battery voltage for a fixed command without compensation. The thrust significantly drops as the battery discharges.

plotted the scatter points of thrust as a function of command and battery voltage after compensation (Figure 3.15). We superimposed a 1-degree plane surface on this graph to highlight the linear behaviour resulting from the compensation.

However, this linearization process does come with a trade-off. In order to ensure symmetry in propeller performance, the maximum thrust was capped at  $14g$ , corresponding to the lesser thrust-generating direction of the propeller. While this means some dynamic range and speed in the forward direction were sacrificed, the benefits outweigh the drawbacks. The resulting model provides better control at lower speeds, which we deemed more critical than having a high-speed blimp.

Overall, the implementation of the compensation algorithm has proven to be highly effective in maintaining the performance of the propulsion system, even under changing battery voltage conditions. This enhances the reliability and utility of our blimp model, providing a solid foundation for further optimization and application.

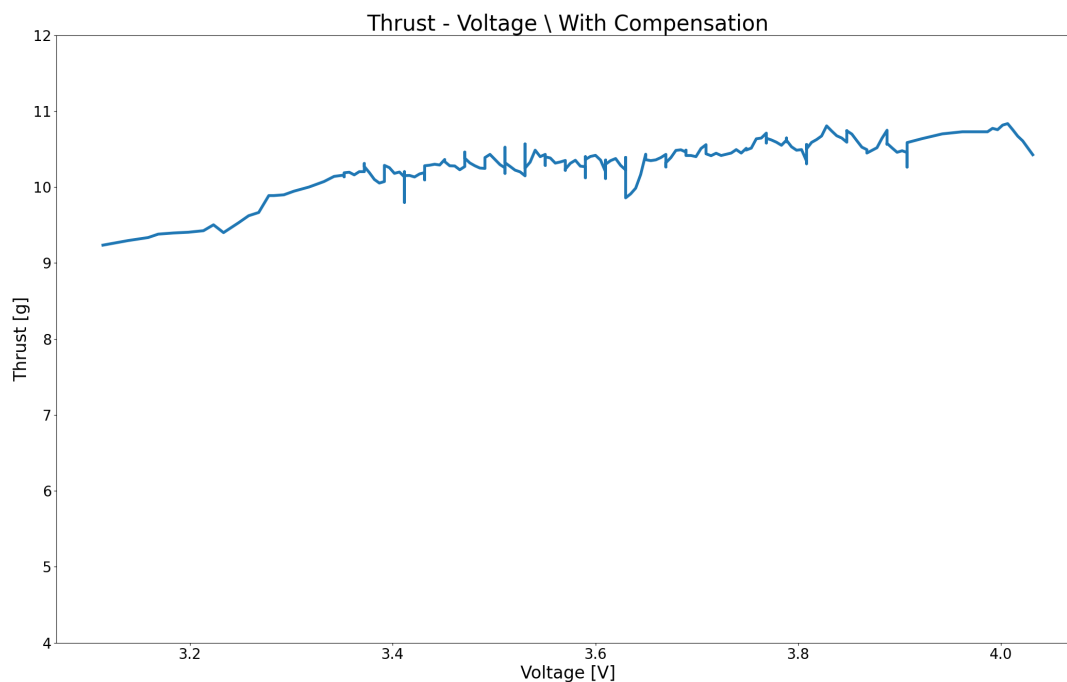


**Figure 3.13:** Thrust output as a function of battery voltage for a fixed command with battery compensation. Despite the battery discharging, the thrust remains nearly constant.

## 3.6 Chapter Summary and Conclusion

This chapter began with a comprehensive discussion of all the sensors involved in the design process of the blimp. Then it moves toward the study of state estimation for our blimp. An extended Kalman filter, an optimal estimator that uses a two-step process – prediction and update – to estimate the current state of a system, was used. The benefit of the extended Kalman filter lies in its ability to handle nonlinearities in system dynamics and measurement models, making it particularly well-suited to the task of state estimation for our blimp. To validate our state estimator, we used a Qualisys motion capture system as a source of 'ground truth', showing the accuracy of our estimates in different scenarios, including forward movement, side slip, and rotation.

Following state estimation, we delved into the details of the PID controller, explaining the structure, which is integral to achieving stable flight for our blimp.

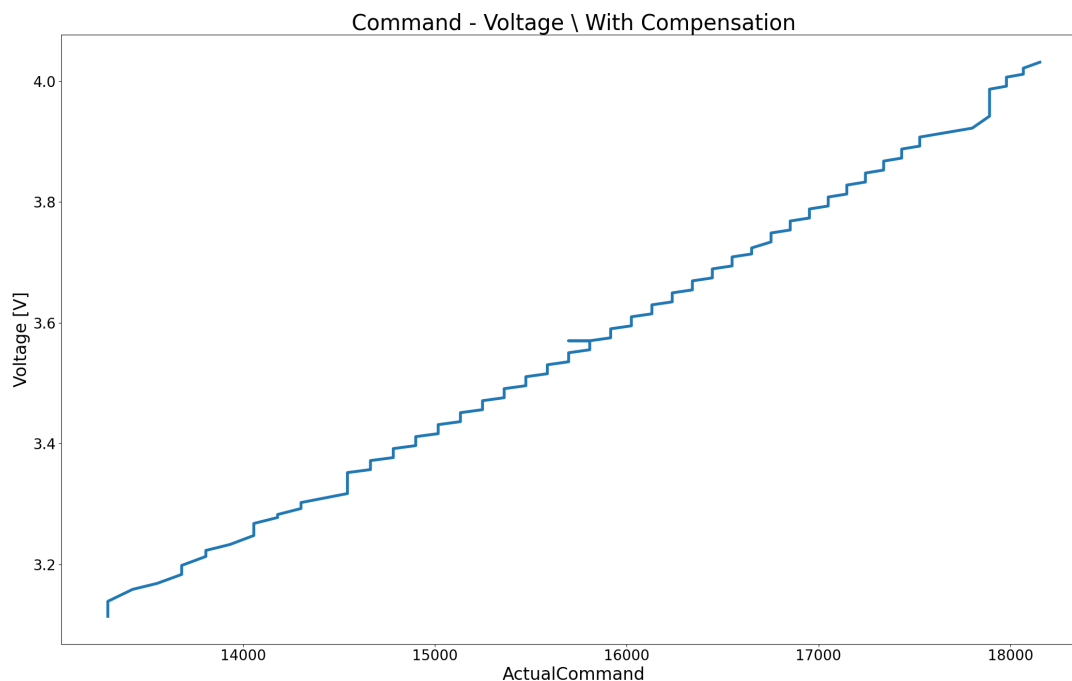


**Figure 3.14:** Changes in command values as a function of battery voltage to maintain near-constant thrust. The compensation algorithm adjusts the command values dynamically to ensure consistent performance.

PID control loops were used to control altitude, yaw, and forward velocity.

We then examined the power distribution block and its importance in system operations. This component is responsible for effectively distributing power from a single battery to multiple motors while ensuring that the direction of thrust is appropriate for the desired motion. Through rigorous experimentation, we studied the different characteristics of various propellers under different commands, enabling us to choose the most efficient propeller.

The final part of the chapter was dedicated to a deep dive into the development and application of our unique battery compensation and linearization algorithm. We recognized that both battery discharge and the non-linear behaviour of the propellers could adversely affect the system's performance. By developing a compensation algorithm, we mitigated these effects and enhanced the overall system's reliability and efficiency. Detailed regression analyses and numerous experiments helped us fine-tune the algorithm and achieve impressive results.

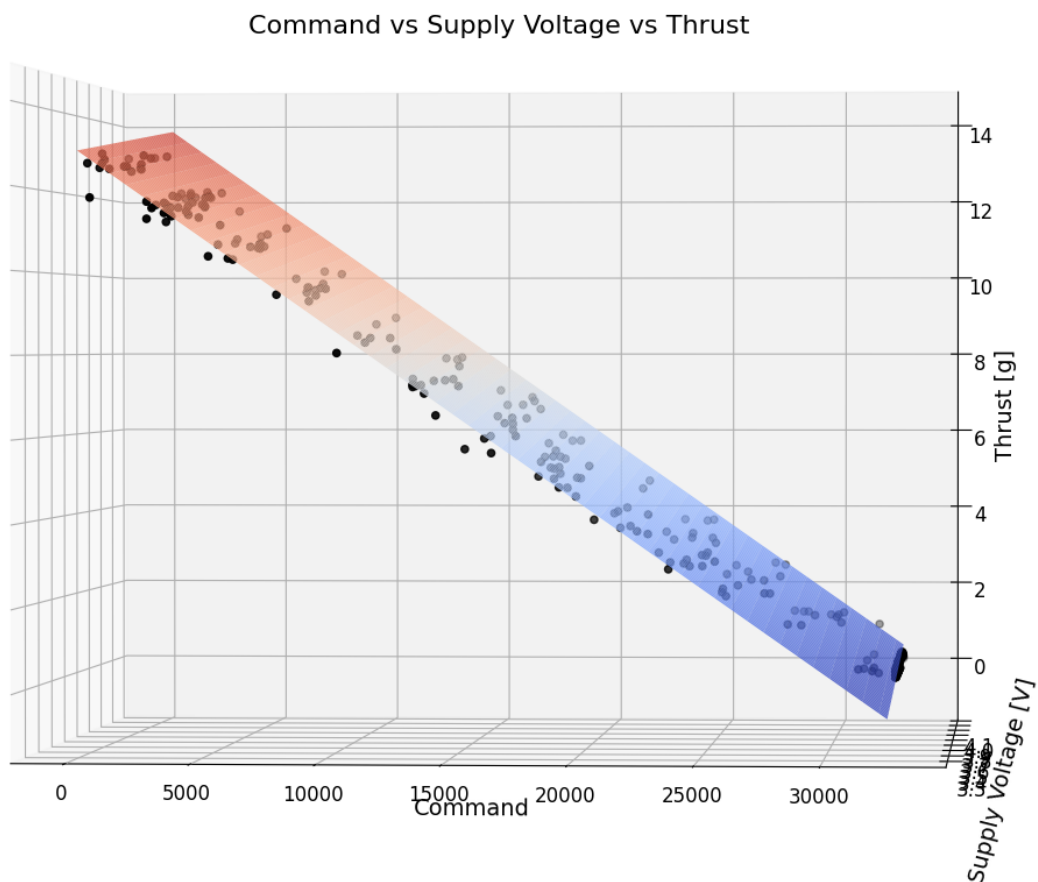


**Figure 3.15:** Post-compensation thrust as a function of command and battery voltage, showing a linear behaviour. The superimposed 1-degree plane surface serves to underscore the linearization achieved.

In conclusion, this chapter has covered the essential components of our blimp’s control system, from state estimation to control and power distribution, all the way to battery compensation and linearization. Each section presented a challenge that we systematically addressed, demonstrating the robustness and adaptability of our design. As we move forward, we believe that this foundation will pave the way for further improvements and novel applications for our blimp model.

In the upcoming concluding chapter, we will explore in-depth the ultimate outcome and performance of the studied blimp, carefully evaluating its effectiveness and identifying crucial components. We will analyze the tuning process and the

various steps involved in transitioning from the initial design to the ultimate version.

## Chapter 4

# Design Processes, Result and Performance Evaluation

In this final chapter, we will delve into the culmination of our research journey, presenting the results, performance evaluation, and the iterative design process that led to the development of our blimp prototype. This journey began with a simple modification of the Crazyflie nano quadcopter, transforming it into a rudimentary blimp. Despite its limitations, this initial prototype served as a proof of concept, demonstrating the feasibility of our project and paving the way for more advanced iterations.

The project took a significant leap forward with the introduction of the Crazyflie Bolt, which allowed us to utilize brushless motors. While these motors consume more power than their brushed DC counterparts, they offered the advantage of bidirectional control, a crucial feature for our blimp. This choice, although not ideal, was a necessary compromise that will inform our future work on the use of bidirectional DC motors.

Our prototyping journey was marked by a series of trials, errors, and improvements. We experimented with different materials for the hull, starting with foil balloons, moving to latex, and finally settling on stretchy plastic balloons. Each choice brought its own set of challenges and advantages, contributing to our understanding of the factors that influence the blimp's performance.

We also embarked on a quest to improve the blimp's battery life, conducting

numerous tests to measure flight time. This led to the development of a Python script for position control and PID Controller tuning, which proved instrumental in refining the blimp's performance.

In this chapter, we will discuss these developments in detail, presenting the results of our tests and the performance of the final prototype. We will also reflect on the lessons learned from this iterative design process and look ahead to future improvements and research directions.

## **4.1 Design and Prototyping**

This section delves into the critical stages of our project: the design and prototyping process. This iterative process was characterized by continuous learning, adaptation, and improvement, culminating in the development of a blimp prototype that fulfilled our research objectives.

The process commenced with a straightforward modification of the Crazyflie nano quadcopter, converting it into a basic blimp. This initial prototype served as a valuable proof of concept, affirming the feasibility of our project and setting the stage for more advanced iterations.

The design and prototyping process can be divided into two main stages. The first stage involved the initial design and development of the first prototype, which included the transition from the Crazyflie to the Crazyflie Bolt and the introduction of brushless motors. The second stage focused on iterative design modifications, including material testing for the blimp's hull, the development of a 3D model for motor support, and the introduction of stretchy plastic balloons.

Each stage presented its own set of challenges and breakthroughs, contributing to our understanding of the factors that influence the blimp's performance. In the following subsections, we will discuss these stages in detail, highlighting the decisions made, the challenges overcome, and the lessons learned.

### **4.1.1 Initial Design and Prototyping**

The initial prototype of the blimp was developed using a standard quadcopter. The motors were arranged such that two of the four motors pointed forward for

propulsion, while the other two were aligned downward for altitude control. This configuration served as the gondola of the blimp. A reference figure illustrating this configuration is presented in Figure 4.1.

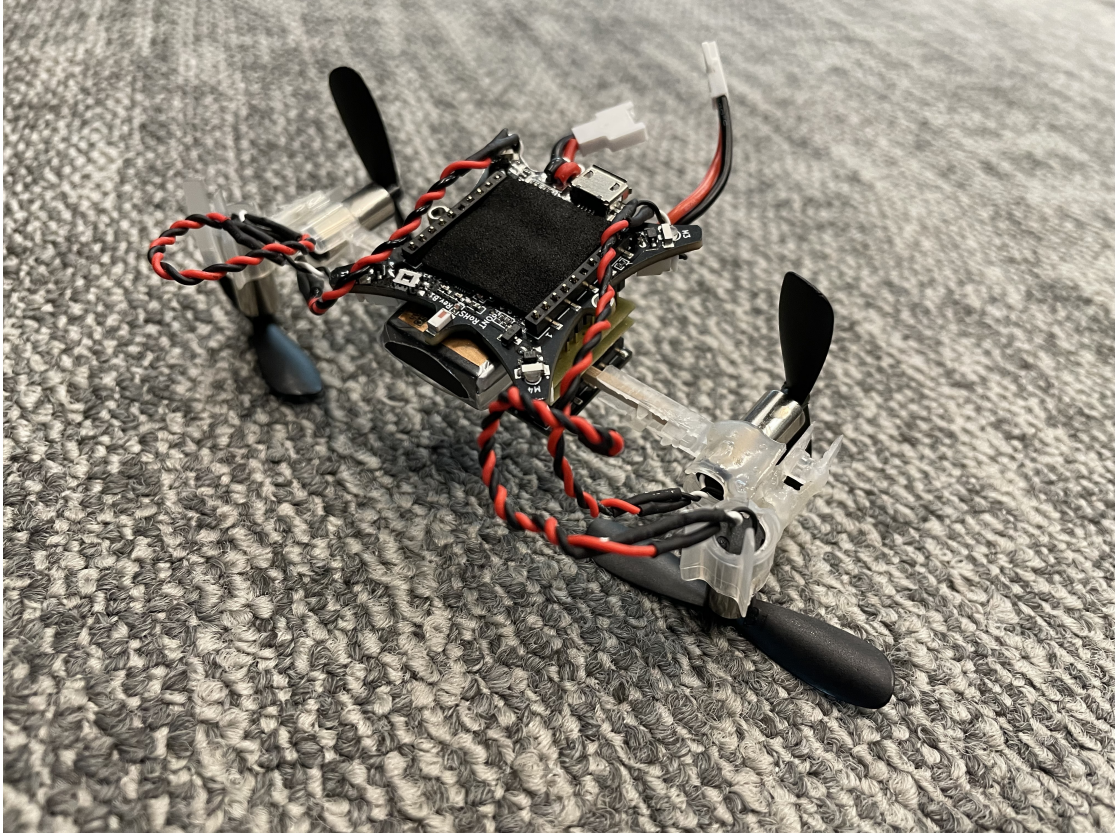


**Figure 4.1:** This first prototype has been made by a rearranging of the motor of a Crazyflie

This initial modification, however, was not sufficient on its own. A modification in the power distribution of the firmware, as described in the previous chapter, was necessary to remap the movement of the blimp with the motors.

With this prototype, we were able to conduct preliminary manual navigation tests using an external control device. For these tests, we used a commercially available controller, chosen for its ergonomic design and intuitive control interface.

The primary objective of these initial tests was to verify the functionality of the altitude control, which was confirmed to be working, albeit in a rudimentary fashion. The major challenge encountered during these tests was related to the

balloon. Our initial calculations for the balloon size did not account for the weight of the balloon itself. Foil balloons, while durable, are quite heavy. For the initial tests, we used three balloons attached to each other. This setup, while functional, was far from ideal, particularly from a stability perspective.

Despite these challenges, the initial prototype demonstrated the feasibility of the project. This marked the beginning of an iterative process of platform improvement, with each iteration building on the lessons learned from the previous one.

### **4.1.2 Iterative Design changes**

As we progressed with our project, the initial blimp prototype underwent several iterations, each one building on the lessons learned from the previous design and bringing us closer to our final prototype. These iterations involved various modifications and improvements, including the transition to the Crazyflie Bolt, adjustments in motor placement, and the development of a custom 3D printed structure for motor housing.

Each iteration represented a step forward in our design process, addressing specific challenges and improving the blimp's performance. In this subsection, we will discuss these design iterations in detail, highlighting the rationale behind each change, the challenges encountered, and the impact of these modifications on the blimp's performance.

#### **First Iteration: Crazyflie Bolt and Brushless Motors**

The first iteration of our design marked the transition to the Crazyflie Bolt, enabling us to work with brushless motors. The smallest brushless motors we found were 8mm x 2mm in size, with a shaft dimension of 1mm. At this stage, we did not focus on selecting the optimal propeller. Instead, we concentrated on finding suitable Electronic Speed Controllers (ESCs) that could drive these motors. After configuring the ESCs for bidirectional operation, we created the first supports for these motors.

The design of this prototype aimed to position motors  $M_2$  and  $M_3$  off-center to prevent them from colliding with objects. The motor supports were handcrafted from pieces of plastic and attached with hot glue. Despite its simplicity, this



**Figure 4.2:** This prototype has the first one made with a crazyflie Bolt

prototype allowed us to conduct several promising tests, including a comparative test with a nano quadcopter following a square trajectory (see Figure 4.3). These tests were conducted without the use of the Qualisys system as a sensor, relying instead on optical flow for performance measurement.

The hull material for this design was a latex balloon, which performed satisfactorily at this stage of prototyping. An image of this prototype is shown in Figure 4.2.

Upon analyzing the trajectory of the blimp, we identified several issues. The trajectory exhibited significant overshooting, attributable to the blimp's intrinsic inertia. While this issue could be partially addressed with more precise tuning, the asymmetry of the motors and propellers also contributed to the problem, adversely affecting the trajectory-following step. Furthermore, the trajectory was not fully reliable due to the accumulation of position error from the optical flow and the

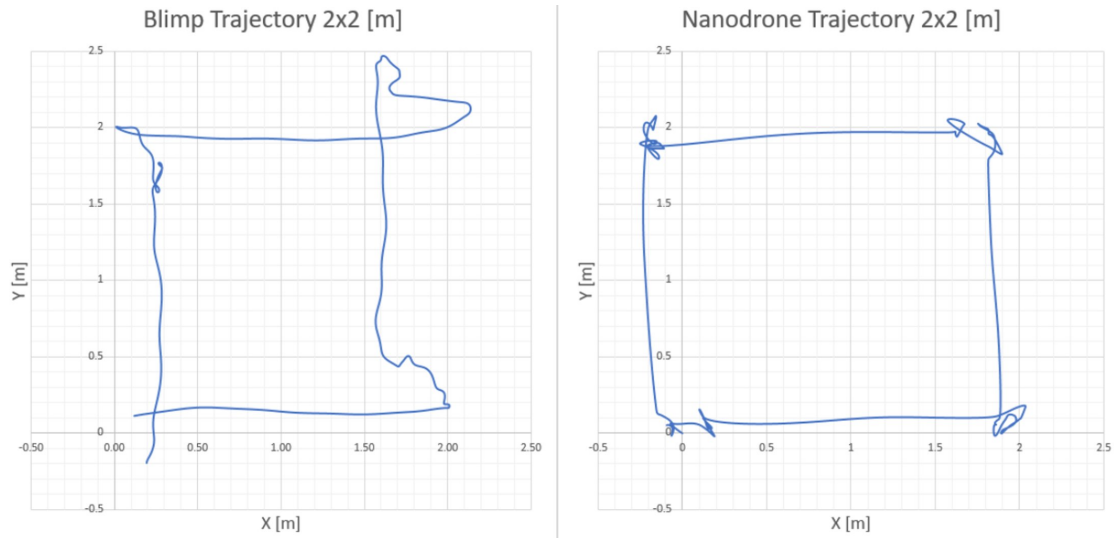


**Figure 4.3:** This image represent the trajectory made by a blimp and a nano quadcopter without involving the use of the Qualisys system.

changing dynamics of the blimp as the battery discharged. These factors presented challenges that the PID Controller could not adequately handle.

Despite the promising results, these issues, along with the problems associated with the handcrafted motor supports and the use of hot glue for attachment, led us to further refine our design in the subsequent iterations.

### **Final Iteration: 3D Printed Frames, Motion Capture System, and Plastic Hull**

In the final iteration of our design, we aimed to address the issues identified in the previous prototypes and refine our design to its optimal form. A significant improvement was the development of 3D printed frames for motor housing and the controller. These frames were designed with weight considerations in mind, aiming to reduce the overall weight of the blimp as much as possible. The material chosen for 3D printing offered the right balance of strength and lightness, making it ideal for our application. Figures 4.5 and 4.4 show the 3D models of these supports.

The support for motors  $M_1$  and  $M_4$  was redesigned to be aligned with the center of the hull. This change was made to prevent pitch rotation and reduce power consumption, as an off-center placement of the motors was found to be detrimental

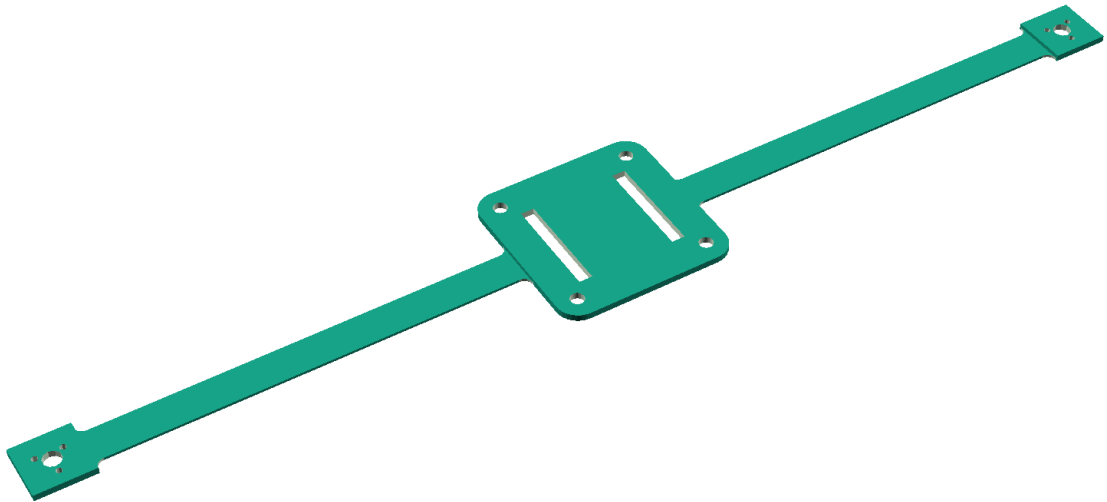


**Figure 4.4:** 3D model of the lower motor support. The design allows for flexibility to conform to the shape of the hull and minimize oscillations during motor operation.

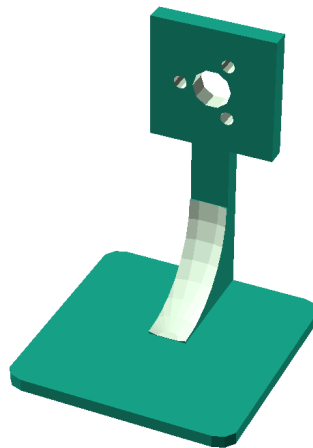


**Figure 4.5:** 3D model of the lateral motor support.

to the overall stability and efficiency of the blimp.

In this iteration, we also decided to use the best-performing propellers identified in our previous analysis. This choice, coupled with the implementation of the battery compensation algorithm discussed in the previous chapters, led to a noticeable improvement in the blimp's performance.

Another significant development was the integration of the motion capture

system. We attached special reflective tape to the hull of the blimp, enabling the motion capture system to track the blimp's position and orientation accurately. This allowed for more precise control and measurement of the blimp's movements, overcoming the limitations of the optical flow used in the previous prototype.

The final major improvement in this iteration was the transition to a plastic material for the hull. This material was chosen for its lightness and durability, making it ideal for our application. The use of a plastic hull marked a significant step forward in the design of our blimp, enhancing its performance and longevity.

These improvements culminated in our final prototype, shown in fig. 4.6, which represented the optimal balance of design considerations and performance requirements. The lessons learned from this iterative design process will serve as valuable insights for future research and development efforts in this field.



**Figure 4.6:** Final prototype of the blimp under study.

## **4.2 Tuning Process**

Tuning is a critical step in the development of control systems. It involves adjusting the parameters of a controller to achieve optimal system performance. In the context of our blimp project, the parameters of interest were the Proportional, Integral, and Derivative (PID) gains of the controller. The tuning process aimed to find the set of PID gains that resulted in the best performance in terms of response speed, stability, and robustness.

### **4.2.1 Development of the Python Script**

To aid the tuning process, we developed a Python script. This script served two primary functions: providing real-time visual feedback on the blimp's position and yaw, and allowing on-the-fly adjustments to the PID parameters of the controller.

The script featured a user-friendly graphical user interface (GUI). This interface allowed us to individually adjust the Proportional, Integral, and Derivative gains, providing us with fine control over the tuning process. The GUI also enabled us to set the desired reference position and yaw for the blimp, facilitating the testing of the blimp's response to different control objectives.

In addition to these features, the Python script also logged data from the tuning sessions. This included the PID gains, the reference and actual position and yaw of the blimp, and the time. This data logging feature was useful for retrospective analysis of the tuning sessions, helping us understand the effects of different PID gains on the system's performance.

Overall, the Python script was a valuable tool in the tuning process. It provided real-time feedback, facilitated PID gain adjustments, and logged data for analysis, contributing to the efficient and effective tuning of the blimp's control system.

### **4.2.2 Theoretical Basis for Tuning**

The tuning process for a PID controller is a critical step in control system design. It involves adjusting the Proportional, Integral, and Derivative gains to achieve an optimal system response. The goal is to find a balance between response speed, overshoot, settling time, and steady-state error.

## **Ziegler-Nichols Tuning Method**

One of the established methods for PID tuning is the Ziegler-Nichols method [11]. This method provides empirical rules for setting the PID gains based on the characteristics of the system's response to a step input. The method involves two steps: first, the integral and derivative gains are set to zero, and the proportional gain is increased until the system starts to oscillate. This gain is known as the ultimate gain,  $K_u$ . The period of the oscillation is the ultimate period,  $T_u$ . The PID gains are then set according to the following rules:

- Proportional control:  $K_p = 0.6K_u$
- PI control:  $K_p = 0.45K_u$ ,  $T_i = 0.83T_u$
- PID control:  $K_p = 0.6K_u$ ,  $T_i = 0.5T_u$ ,  $T_d = 0.125T_u$

While the Ziegler-Nichols method provides a good starting point, it often requires further fine-tuning to achieve optimal performance. In our project, we used a more heuristic approach, involving a combination of manual tuning and trial-and-error.

## **4.3 Detailed Examination of Autonomous Flight Outcomes**

In this section, we will delve into the analysis of our findings, revealing the robust performance of the blimp under study. Our design and tuning process yielded significant results in areas of trajectory tracking, altitude maintenance, and flight duration.

### **4.3.1 Trajectory Analysis**

Figure 4.7 presents the blimp's performance when following a squared trajectory, executed multiple times to evaluate its reliability.

Although the plotted trajectory is not flawless, considering the complexities involved in operating the blimp, the achieved accuracy is highly commendable. Remarkably, the blimp can move laterally while maintaining a constant orientation,

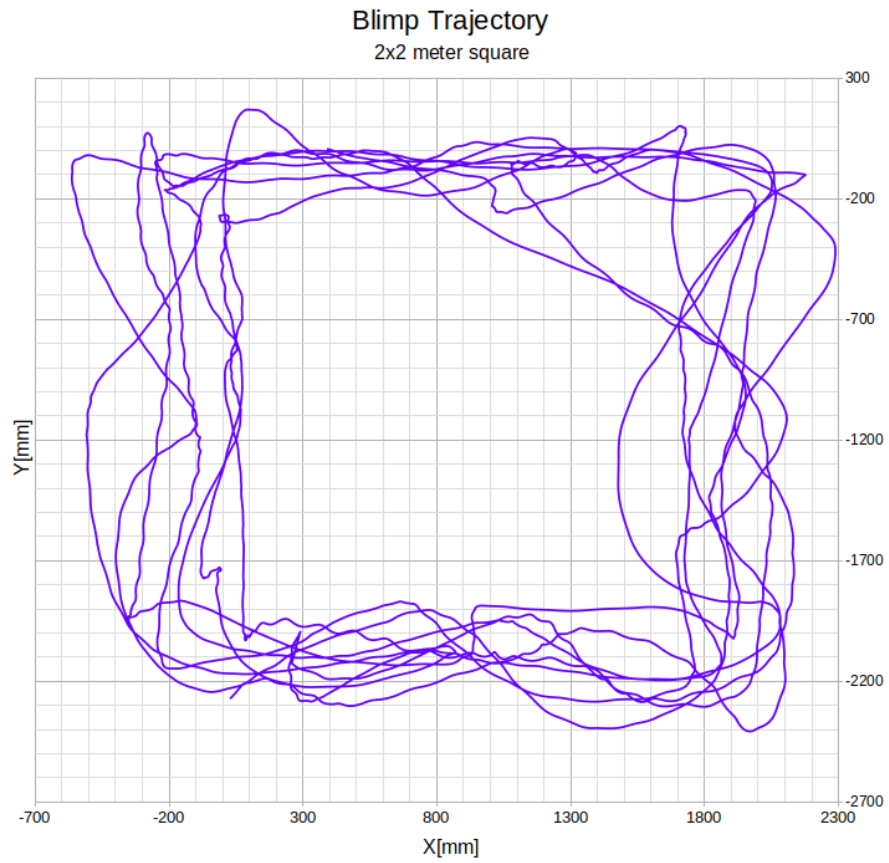


**Figure 4.7:** Squared Trajectory of the Blimp

suggesting a superior navigational mechanism compared to the common method of turning and moving forward.

Even though a few trajectories diverged at specific points, the blimp's ability to recover and return to the prescribed path is significant. Disturbances such as minor air movements, or potential communication issues between the control system and the blimp, could contribute to these deviations. Further tuning of the PID controller and refining the motor placement could potentially rectify these minor deviations.

### 4.3.2 Altitude Maintenance

We also assessed the blimp's ability to maintain a consistent altitude. Figure 4.8 represents the altitude variation over time during the trajectory tracking.

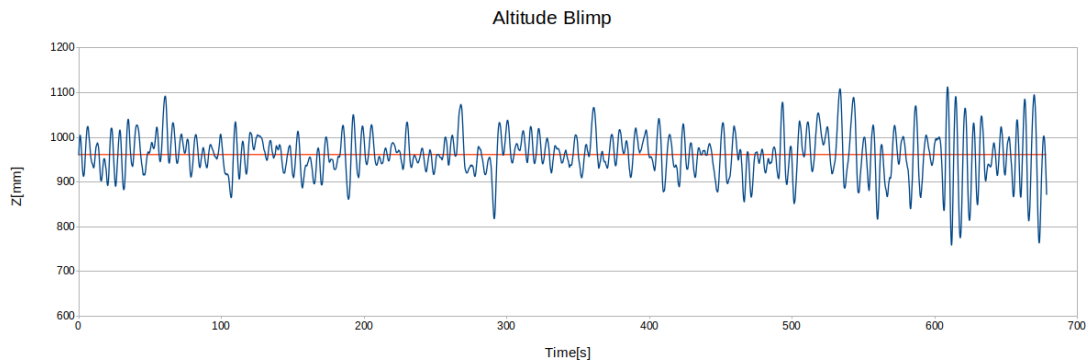


**Figure 4.8:** Altitude Variation over Time

Despite the inherent noise, which is depicted as oscillations, the blimp tracked the intended altitude exceptionally well. With a hull height of 70 cm, the blimp maintained a nearly perfect altitude of 0.96 m. The oscillations increased towards the end of the trajectory, most likely due to battery power depletion. This event marks the limit of our current battery compensation algorithm, which leads to higher oscillations as the motors slow down and the battery voltage drops.

Addressing these challenges could involve using motors with less current draw or batteries capable of delivering higher currents, which could help to maintain the trajectory even during later stages of the battery life.

### **4.3.3 Flight Duration**

The blimp's extended flight duration, exceeding 10 minutes on a single battery charge, is a significant achievement. Such duration is astonishing compared to a nano-quadcopter using the same 600mAh battery, which can only manage a flight of 5 minutes, or a mini quadcopter, which flies for only 15 minutes using a battery that is ten times larger. These comparisons underline the blimp's extraordinary power efficiency and suggest a promising avenue for further enhancing its motion capability and flight duration.

In hover conditions, the blimp sustained its flight for an astounding 14 minutes. Such a capability holds considerable potential for applications like advertising, where prolonged exposure is beneficial. By reducing the aggression of the PID controller, a slight decrease in position tracking accuracy can further increase the hovering duration, offering an excellent trade-off for specific use cases.

### **4.3.4 Robustness and Scalability**

A noteworthy aspect of our results is the robustness of the blimp's performance. It has been tested under different indoor environmental conditions, such as changes in temperature and air quality. Despite these fluctuations, the blimp has consistently followed the prescribed trajectory, indicating a high degree of robustness to environmental variation.

Moreover, the design of the blimp and the control system shows scalability potential. The current design based on a 70 cm hull can be scaled up for larger blimps or scaled down for smaller ones without significant degradation in performance. This scalability can open up new opportunities for its use in different scenarios, from small indoor spaces to larger outdoor areas, broadening the range of potential applications.

### **4.3.5 Real-world Applicability**

Lastly, we explored potential real-world applications for our blimp design. Given its prolonged hovering ability, one application area could be advertising or event coverage, where the blimp could carry a display or camera system.

Additionally, the blimp's ability to navigate reliably while maintaining its orientation and altitude could be applied in areas such as inspection tasks or environmental monitoring. Its low power consumption and quiet operation would be particularly advantageous in noise-sensitive environments.

This broad spectrum of potential applications indicates that the results obtained from our study have far-reaching implications beyond the specific context of blimps, contributing significantly to the broader field of autonomous systems.

### **4.3.6 Limitations**

1. **External Disturbances:** The blimp's stability is an ongoing concern that requires further improvement. In challenging and constrained situations, the blimp's ability to navigate reliably can be compromised. To address this limitation, a more comprehensive analysis of the blimp's dynamics is necessary, leading to more accurate tuning of the control system. This would ensure better stability and maneuverability, particularly in adverse environmental conditions.

2. **Brushless Motor Performance:** The aggressive behavior of the brushless motors used in the blimp can result in abrupt movements, affecting overall stability and control. Future research should focus on fine-tuning the motor parameters, such as throttle response and control gains, to achieve smoother and more controlled movements. Additionally, optimizing the power consumption of the motors could be explored to improve overall energy efficiency.

3. **Suitability of the Qualisys System:** While the Qualisys motion capture system served the purpose for this study, it may not be suitable for all scenarios. The reliance on an external tracking system limits the blimp's flexibility and usability in environments where the system is not available or feasible. Future work could investigate alternative sensing and localization methods, such as onboard sensors or computer vision algorithms, to enhance autonomy and reduce reliance on external tracking systems.

4. **Roll Movement and Camera Stability:** The lateral movement of the blimp can induce a roll motion, which could impact camera stability during operations that require steady footage or image capture. Addressing this limitation would involve exploring additional mechanisms or control strategies to minimize or compensate for undesired roll movements, ensuring smoother camera operation

and improved stability during lateral maneuvers.

**5. Motor Protection and Collision Avoidance:** The blimp's motors currently lack proper housing or protection, which leaves them vulnerable to collisions or other potential damage. Future research should focus on implementing suitable motor housings or protective measures to enhance the blimp's durability and prevent mechanical failures that could affect flight performance and overall reliability.

These additional limitations further emphasize the need for ongoing research and development to address stability issues, optimize motor behavior, explore alternative sensing methods, improve camera stability, and enhance overall robustness through protective measures. Despite these limitations, the blimp's successful trajectory following, impressive altitude maintenance, and long flight duration showcase the progress made thus far and highlight the potential for continued advancements in the field of autonomous blimps.

#### **4.3.7 Future Work**

**Disturbance Rejection:** Future work should focus on developing advanced control strategies to enhance the blimp's reliability and robustness against external disturbances. This could involve implementing adaptive or robust control methodologies, such as model predictive control or disturbance observer-based control, to handle various environmental factors. Additionally, incorporating machine learning techniques, such as reinforcement learning or adaptive control algorithms, could enable the blimp to learn from and adapt to changing environments, further improving disturbance rejection capabilities.

**Power Optimization:** Future research should delve deeper into optimizing the power management system of the blimp. This could involve exploring alternative types of motors or batteries that offer improved energy efficiency. For example, investigating the use of low-power consumption DC motors or considering alternative power sources like solar panels or fuel cells could enhance the blimp's endurance and reduce reliance on traditional battery technology. Moreover, improving the battery compensation algorithm by developing more accurate models or adaptive control algorithms could further optimize power consumption. Additionally, the development of an energy-aware flight planning system that takes into account the remaining battery charge and adjusts the trajectory or control parameters

accordingly could extend the blimp's mission duration.

**Mission-adaptable Control Strategies:** The study highlighted differences in performance based on the blimp's operational mode, specifically trajectory following and hovering. Future research could focus on developing mission-adaptable control strategies that can be customized to meet specific mission requirements. This could include the implementation of energy-saving modes to optimize battery usage during long-duration flights or precision-oriented control modes for tasks that demand high accuracy. Additionally, a combination of both modes could be explored to achieve a balance between energy efficiency and precise control, allowing the blimp to adapt its behavior based on the mission objectives and constraints.

By addressing these areas of future work, the blimp's reliability, power efficiency, and adaptability can be significantly enhanced. These research directions pave the way for the development of more capable and versatile autonomous blimps that can operate robustly in dynamic environments and fulfill a wide range of mission requirements.

# Conclusion

In this thesis, we set out to explore the potential of miniature indoor blimps as a safer, quieter, and more resilient alternative to traditional quadcopters for indoor navigation. Our research problem was centered around the design and control of these blimps, with a focus on enhancing their spatial control, trajectory-following capabilities, and safety features, while also extending their flight times.

We began our journey by delving into the theoretical aspects of the blimp design, including kinematic and dynamic modelling. We made certain assumptions for a simplified model and discussed the schematic structure of the blimp. This theoretical foundation allowed us to understand the unique attributes of blimps and how they could be leveraged to overcome the challenges associated with quadcopters in indoor environments, such as safety risks, noise generation, and energy constraints.

Following this, we moved into the practical aspects of the blimp design. We discussed sensor selection, state estimation with a Kalman filter, PID controller design, and power distribution. We also introduced a battery compensation and linearization technique to maintain near-constant thrust. These design and implementation steps were crucial in enhancing the blimp's spatial control, trajectory-following capabilities, and safety features.

Finally, we presented the design and prototyping process, including iterative design changes. We discussed the tuning process and provided a detailed examination of autonomous flight outcomes, including trajectory analysis, altitude maintenance, flight duration, robustness, scalability, and real-world applicability.

However, our research was not without limitations. One of the limitations lies in the battery compensation and linearization technique. While it has been successful in maintaining near-constant thrust, the development of more accurate

models or adaptive control algorithms could enhance this aspect of the blimp's performance. Another area for improvement is the implementation of energy-saving modes for long-duration flights. While the blimp's ability to remain airborne for extended periods is a significant advantage, the development of energy-saving modes could further extend the flight times and make the blimp even more suitable for long-duration tasks. Additionally, the development of mission-adaptable control strategies could enhance the blimp's adaptability. While our design has shown robustness and scalability, the development of control strategies that can adapt to different mission requirements could make the blimp more versatile and capable of operating robustly in dynamic environments.

The implications of this research are manifold and have the potential to significantly impact both the academic field and practical applications. The indoor blimp presents a safer, quieter, and more resilient alternative to traditional quadcopters for indoor navigation. Its unique attributes, such as the ability to remain airborne for extended periods, tolerance to minor impacts, and quieter operational noise level, make it particularly suitable for long-duration tasks in indoor environments. These features could have significant implications for various applications, including surveillance, logistics, and environmental research.

Furthermore, the research identifies several areas for future work that could further enhance the blimp's reliability, power efficiency, and adaptability. These include the development of more accurate models or adaptive control algorithms for battery compensation, the implementation of energy-saving modes for long-duration flights, and the development of mission-adaptable control strategies. Addressing these areas could pave the way for the development of more capable and versatile autonomous blimps that can operate robustly in dynamic environments and fulfill a wide range of mission requirements.

In conclusion, our work in this thesis offers a comprehensive exploration of the potential of miniature blimps as indoor exploration vehicles. We have shown that they hold compelling advantages over traditional quadcopters, including superior spatial control, trajectory-following capabilities, extended flight times, and increased safety features. We hope that our findings contribute to the broader discourse on unmanned aerial vehicles (UAVs) and inspire further research and innovation in the field of indoor aerial vehicles. The indoor blimp, with its unique attributes and

advantages over traditional quadcopters, presents a promising avenue for future exploration. Despite the limitations acknowledged, the potential of this technology is vast. The areas for improvement we identified not only provide opportunities for future research but also highlight the potential for further innovation in the field of indoor aerial vehicles.

Our research has shown that the indoor blimp is not just a theoretical concept but a practical solution with real-world applicability. Its superior spatial control, trajectory-following capabilities, extended flight times, and increased safety features make it a compelling alternative for indoor navigation tasks.

Moreover, the implications of our findings extend beyond the academic field. The indoor blimp could revolutionize various practical applications, including surveillance, logistics, and environmental research, by providing a safer, quieter, and more resilient solution for indoor navigation.

In light of our findings, we believe that the indoor blimp deserves further attention and research. We hope that our work inspires other researchers to explore this promising technology further and continue the innovation in the field of indoor aerial vehicles.

In conclusion, our journey from the conceptualization of the indoor blimp to its final implementation has been both challenging and rewarding. We believe that our work contributes significantly to the broader discourse on unmanned aerial vehicles (UAVs) and sets the stage for future research and innovation in the field of indoor aerial vehicles.

# Bibliography

- [1] Hazim Shakhatreh, Ahmad H. Sawalmeh, Ala Al-Fuqaha, Zuochao Dou, Eyad Almaita, et al. «Unmanned aerial vehicles (uavs): a survey on civil applications and key research challenges». In: (2019), pp. 48572–48634 (cit. on p. 5).
- [2] Li Y., Nahon M., and Sharf I. «Airship dynamics modeling: A literature review». In: (2011), pp. 217–239 (cit. on p. 7).
- [3] M. Burri et al. «Design and control of a spherical omnidirectional blimp». In: (2013), pp. 1873–1879. DOI: 10.1109/IR0S.2013.6696604 (cit. on p. 8).
- [4] Thor I.Fossen. *Guidance of ocean vehicles*. Wiley, 1994 (cit. on p. 9).
- [5] S. B. V. Gomes. *An investigation of the Flight Dynamics of Airship with Application to the YEZ-2A*. 1990 (cit. on p. 10).
- [6] Wayne Johnson. *Rotorcraft Aeromechanics*. Cambridge University Press, 2013 (cit. on p. 47).
- [7] G. Frey and A. Adkins. «Design, Fabrication, and Testing of a Small Variable-Pitch Quadrotor». In: *International Journal of Micro Air Vehicles* (2015) (cit. on p. 48).
- [8] A. Betz. *Aerodynamics of Propellers*. McGraw-Hill, 1927 (cit. on p. 48).
- [9] B. W. McCormick. *Aircraft Propeller Design*. McGraw-Hill, 1937 (cit. on p. 48).
- [10] Ira H. Abbott, Albert E. von Doenhoff, and Louis S. Stivers Jr. *Summary of Airfoil Data*. Tech. rep. NACA, 1959 (cit. on p. 48).
- [11] J. G. Ziegler and N. B. Nichols. «Optimum settings for automatic controllers». In: *Transactions of the ASME* 64 (1942), pp. 759–768 (cit. on p. 72).